

学位論文

Material Circulation in the  
Venus Atmosphere

金星大気における物質循環

平成9年12月 博士(理学)申請

東京大学大学院理学系研究科  
地球惑星物理学専攻

今村 剛

0  
学位論文

Material Circulation in the  
Venus Atmosphere

金星大気における物質循環

平成9年12月 博士（理学）申請

東京大学大学院理学系研究科  
地球惑星物理学専攻

今村 剛

## Abstract

In the past a few decades the theories of the Venus atmospheric chemistry and cloud physics have been developed focussing exclusively on the vertical structure. In those theories the horizontal structure was ignored and the transport processes were taken into account in the form of vertical eddy diffusion, although a vigorous meridional circulation is evident from observations. In the present thesis, Chapters 2-4 shed light on the large-scale meridional circulation in the Venus atmosphere, and Chapter 5 discusses the dissipation process of gravity waves which is important in determining the relative importance of large-scale circulation and eddy diffusion.

In Chapter 2, the cloud formation in the middle atmospheric circulation is discussed. A two-dimensional model study revealed that the meridional circulation has a large influence on the distributions of the cloud and condensable gases on Venus. In the model, the observed depression of near-infrared optical thickness at mid-latitude is reproduced as a result of the enhancement of cloud thickness at low and high latitudes. At high latitudes, the poleward transport of  $\text{H}_2\text{SO}_4\text{-H}_2\text{O}$  droplets in the upper atmosphere makes a thick cloud, since most of the  $\text{H}_2\text{SO}_4\text{-H}_2\text{O}$  droplets photochemically produced are transported poleward by the meridional circulation. At low latitudes, the large-scale ascent of the concentrated  $\text{H}_2\text{SO}_4$  vapor forms the dense lower cloud observed by entry probes. The equatorward transport of  $\text{H}_2\text{SO}_4$  vapor below the cloud by the meridional circulation and the sedimentation of droplets in the lower cloud leads to the accumulation of  $\text{H}_2\text{SO}_4$  vapor around the cloud base at low latitudes. The accumulation of  $\text{H}_2\text{SO}_4$  vapor at low latitudes agrees with the radio occultation observations. The middle cloud is caused by the condensation of  $\text{H}_2\text{SO}_4$  vapor transported upward from below by convective mixing.

In Chapter 3, the momentum balance of the middle atmospheric circulation is discussed. The downward control principle is applied to estimate the vertically integrated zonal force driving the mid-latitude mesosphere. The distinct localization of the forcing in the mid-latitude implies that Rossby or gravity waves will be the momentum carrier. Rough estimates of the Eliassen-Palm flux suggest that the meridional circulation will be driven principally by a Rossby wave, although the contribution of gravity waves cannot be ruled out. It is also shown that the variation of the jet intensity with a time scale of several years is consistent with the variation of Rossby wave activity. Advective transport is as important as eddy diffusion for tracer transport in the middle atmosphere.

In Chapter 4, the circulation in the lower atmosphere is discussed. The intensity of the surface direct cell, whose existence is indicated by the aeolian features observed by

the Magellan spacecraft, is inferred from the radiative energy balance at each latitude and the static stability observed. The typical meridional flow speed is estimated to be a few  $\text{cm s}^{-1}$ . Then, the advection time scale is much longer than the planetary rotation period and comparable to the radiative relaxation time. The estimated circulation speed and the observed latitudinal temperature contrast yield the net upward heat transport by the cell of several  $\text{W m}^{-2}$ , which may have caused the stable stratification observed. It is also suggested that atmospheric constituents are transported mostly by the cell rather than by eddy diffusion in the lower atmosphere.

In Chapter 5, the radiative damping of gravity waves and the consequent decrease of wave-induced turbulent diffusion are investigated for the upper atmospheres of terrestrial planets. The radiative damping due to the  $\text{CO}_2$   $15 \mu\text{m}$  radiation limits wave propagation much more effectively in the Mars atmosphere than in the Earth's atmosphere. Radiative damping is more effective than molecular diffusion below 80 km altitude on the Earth, below 120 km altitude on Mars and even above 120 km altitude on Venus. It was also demonstrated that turbulent diffusion can be weakened significantly by radiative damping in the Mars upper atmosphere.

# Contents

Abstract	i
<b>1 General introduction</b>	<b>3</b>
<b>2 Venus cloud formation in the meridional circulation</b>	<b>6</b>
2.1 Introduction	6
2.2 Chemical processes	7
2.3 Transport processes	8
2.3.1 Meridional circulation	8
2.3.2 Particle sedimentation	9
2.3.3 Eddy diffusion	10
2.4 Model descriptions	11
2.4.1 Atmospheric structure, boundary condition and initial condition	11
2.4.2 Production and decomposition of $\text{H}_2\text{SO}_4$ vapor	11
2.4.3 Transport processes	12
2.4.4 Condensation and evaporation of $\text{H}_2\text{SO}_4$ and $\text{H}_2\text{O}$	17
2.5 Model results	18
2.5.1 Cloud structure	18
2.5.2 $\text{H}_2\text{SO}_4$ vapor	22
2.5.3 $\text{H}_2\text{O}$ vapor	25
2.6 Discussions and Conclusions	28
<b>3 Momentum balance of the Venus mid-latitude mesosphere</b>	<b>30</b>
3.1 Introduction	30
3.2 Zonal force requirement	31
3.3 Mid-latitude Rossby wave	34
3.3.1 Eliassen-Palm flux associated with Rossby wave	34

3.3.2	Suppression of mid-latitude jets by wave-driven circulation . . . . .	35
3.4	Internal gravity waves . . . . .	38
3.5	Conclusions . . . . .	39
<b>4</b>	<b>Heat transport in the deep Venus atmosphere</b> . . . . .	<b>42</b>
4.1	Introduction . . . . .	42
4.2	Estimation of circulation speed . . . . .	43
4.2.1	Potential temperature flux . . . . .	43
4.2.2	Solar radiation . . . . .	45
4.2.3	Thermal radiation . . . . .	45
4.2.4	Static stability . . . . .	47
4.2.5	Result . . . . .	47
4.3	Upward dynamical heat transport . . . . .	49
4.4	Implications for superrotation . . . . .	49
4.5	Conclusions . . . . .	51
<b>5</b>	<b>Radiative damping of gravity waves and turbulence in the upper atmospheres of terrestrial planets</b> . . . . .	<b>52</b>
5.1	Introduction . . . . .	52
5.2	Radiative damping rate . . . . .	53
5.2.1	Method . . . . .	53
5.2.2	Result . . . . .	54
5.3	Limit of amplitude growth . . . . .	56
5.4	Suppression of turbulence by radiative damping . . . . .	56
5.5	Conclusions . . . . .	58
	<b>Acknowledgements</b> . . . . .	<b>61</b>
	<b>References</b> . . . . .	<b>62</b>

# Chapter 1

## General introduction

We do not have a complete picture of the general circulation of the Venus atmosphere, although observational data have been compiled from decades of observations made from earth and from Mariner, Venera, Pioneer Venus, Vega, Magellan and Galileo spacecrafts. The difficulty of revealing the general circulation arises from the fact that the meridional circulation speed is too slow to be distinguished from the winds associated with atmospheric waves. The meridional circulation structure below the cloud deck was inferred from the meridional winds observed by Pioneer Venus probes [Schubert, 1983], but the inferred circulation structure disagrees with the mean advection direction around 50 km altitude determined from the cloud motions in near-infrared images [Belton *et al.*, 1991; Carlson *et al.*, 1991].

The circulation structure has partly been revealed exclusively by remote soundings. The poleward character of the mean meridional circulation is evident at  $\sim 65$  km altitude from UV cloud images [Del Genio and Rossow, 1990] and at  $\sim 50$  km altitude from near-infrared cloud images [Belton *et al.*, 1991; Carlson *et al.*, 1991], thus the altitude level of the return flow is lower than  $\sim 50$  km. Such a circulation structure can be inferred also from temperature and trace gas distributions. The observed mesospheric (60–90 km) temperatures are warmer in the polar region and cooler in the equatorial region than radiative equilibrium temperatures, indicating a global-scale meridional circulation with large-scale ascent at low latitudes and descent at high latitudes [Taylor *et al.*, 1983]. Near-infrared spectrometric measurements showed that CO mixing ratio increases by  $\sim 35\%$  north of  $47^\circ\text{N}$  at 30–50 km altitudes, implying that CO formed by the photolysis of  $\text{CO}_2$  above the cloud is transported downward by the descending branch of the meridional circulation at high-latitudes [Collard *et al.*, 1993].

Though a vigorous meridional circulation is evident, its effects on material transport

have been ignored in the models of photochemistry and cloud formation [Winick and Stewart, 1980; Yung and DeMore, 1982; Krasnopolsky and Parshev, 1981, 1983; Krasnopolsky and Pollack, 1994; James et al., 1997]. Since atmospheric constituents are transported vertically by large-scale meridional circulation as well as by small-scale turbulences [e.g., Garcia and Solomon, 1985], the eddy diffusion coefficient in one-dimensional models should represent the meridional circulation as well as turbulence. In the above mentioned models, however, the eddy diffusion coefficient was taken from the turbulence intensity derived from radio scintillation measurements [Woo and Ishimaru, 1981] and the transport by the meridional circulation was not considered. The effect of the meridional circulation on cloud formation and trace gas distributions will be investigated in Chapter 2.

The conservation of angular momentum at each latitude requires deceleration acting on the zonal flow in the poleward circulation around and above the cloud level [Hou and Goody, 1989]. The mechanisms that cause such a deceleration in the Venus atmosphere are unknown. The friction due to small-scale turbulence cannot induce forces strong enough to drive the meridional circulation observed [Imamura, 1997]. In the terrestrial stratosphere, Rossby and gravity waves generated in the troposphere induce zonal forces on the mean flow. The forces drive a global-scale extratropical fluid-dynamical suction pump which withdraws air upward and poleward from the tropical troposphere and pushes it poleward and downward into the extratropical troposphere [e.g., Holton et al., 1995]. It would be reasonable to expect the same mechanism to work on Venus. The validity of the concept of "wave-driven circulation" in the Venus atmosphere will be examined in Chapter 3.

In the lower atmosphere, direct cells are expected to extend to the poles after the aeolian features in the Magellan radar images [Greeley et al., 1992, 1995]. The vertical extent and the intensity of the cell are, however, unknown. Since the Venus atmosphere is not at thermochemical equilibrium even in the lowest scale height [Fegley et al., 1997], the chemical composition must depend on the transport timescale; therefore, further development of the Venus atmospheric and surface chemistry requires the knowledge of the meridional circulation near the surface. A diagnostic analysis was performed by Hou and Goody [1989] to reveal the circulation in the lower atmosphere, but the result conflicts with observations as described in Section 4.1. The transport timescale and the dynamical heat transport in the lower atmosphere will be diagnosed from observed temperatures and radiative fluxes with a new method in Chapter 4.

Both turbulence and meridional circulation are thought to be driven mostly by upward-propagating gravity waves in the terrestrial upper atmosphere [e.g., Garcia and Solomon,

1985], and a similar mechanism is expected to work in the Venus thermosphere [Zhang and Bougher, 1996]. The role of gravity waves in the material circulation depends on dissipation processes: the waves dissipating due to radiative damping or molecular viscosity decelerate the zonal wind to drive the meridional circulation without generating turbulence, while convectively-breaking waves do generate turbulence. Since the composition of thermosphere is sensitive to the altitude of turbopause, atmospheric escape rates also depend on the gravity wave activity and the wave dissipation processes. It is necessary to clarify the dissipation processes of gravity waves for the understanding of both short-term and long-term material transports. The radiative damping of gravity waves in the non-LTE (local thermodynamic equilibrium) regions of the CO<sub>2</sub> atmospheres of Mars and Venus has not been studied. The effects of radiative damping on gravity waves and wave-driven turbulence will be assessed in Chapter 5.

### 3.1 Introduction

The first part of this chapter is devoted to a review of the current status of the study of gravity waves in the thermosphere. The second part of the chapter is devoted to the study of gravity waves in the thermosphere. The third part of the chapter is devoted to the study of gravity waves in the thermosphere. The fourth part of the chapter is devoted to the study of gravity waves in the thermosphere. The fifth part of the chapter is devoted to the study of gravity waves in the thermosphere. The sixth part of the chapter is devoted to the study of gravity waves in the thermosphere. The seventh part of the chapter is devoted to the study of gravity waves in the thermosphere. The eighth part of the chapter is devoted to the study of gravity waves in the thermosphere. The ninth part of the chapter is devoted to the study of gravity waves in the thermosphere. The tenth part of the chapter is devoted to the study of gravity waves in the thermosphere.

## Chapter 2

# Venus cloud formation in the meridional circulation

### 2.1 Introduction

The Venus cloud consists of a main cloud deck at 45–70 km altitudes, accompanied by thinner hazes above and below. The major material of the main cloud deck is thought to be  $\text{H}_2\text{SO}_4$ - $\text{H}_2\text{O}$  droplets, although the existence of solid particles cannot be dismissed [e.g., *Esposito et al.*, 1983]. The life cycle of the cloud particles in the Venus atmosphere has been inferred from the vertical structure of the cloud layer revealed by the particle size spectrometer on board the Pioneer Venus probe [*Knollenberg and Hunten*, 1980]. The  $\text{H}_2\text{SO}_4$  vapor photochemically produced near the cloud top condenses into  $\text{H}_2\text{SO}_4$ - $\text{H}_2\text{O}$  droplets, which are transported downward through sedimentation. The droplets evaporate in the hot lower atmosphere, and  $\text{H}_2\text{SO}_4$  vapor is thermally decomposed to  $\text{SO}_3$  and  $\text{H}_2\text{O}$ . *Krasnopolsky and Pollack* [1994] developed a one-dimensional model for the  $\text{H}_2\text{SO}_4$ - $\text{H}_2\text{O}$  system in the Venus atmosphere. They argued that the large gradient of the  $\text{H}_2\text{SO}_4$  vapor mixing ratio near the cloud base drives an upward diffusion flux of  $\text{H}_2\text{SO}_4$  vapor, which condenses into the dense lower cloud observed by entry probes. This conclusion was obtained also by *Hashimoto* [1996] and *James et al.* [1997] with one-dimensional models. *Hashimoto* [1996] investigated the dependence of the cloud structure on atmospheric parameters and discussed the climate evolution.

The above one-dimensional model results seem to be plausible, but the transport by the meridional circulation (direct cell) will also be important. Around the cloud top, the cloud tracking of UV images indicates a poleward advection with a time scale of 10–100 d ( $d =$

earth days) [Del Genio and Rossow, 1990] and the deviation of observed temperatures from radiative equilibrium [Crisp, 1989] implies the advective exchange time of  $\sim 90$  d [Imamura, 1997]. On the other hand, as shown later in Section 2.3.2, it takes about 200 d to fall a scale height of 6 km for the Mode 2 particles that are dominant by weight in the upper cloud region. Therefore, the  $\text{H}_2\text{SO}_4\text{-H}_2\text{O}$  droplets produced near the cloud top are transported poleward by the meridional circulation without effective removal by sedimentation. The latitude dependences of cloud thickness [Crisp *et al.*, 1991] and  $\text{H}_2\text{SO}_4$  vapor distribution [Jenkins and Steffes, 1991] may imply the importance of the meridional circulation in the cloud formation.

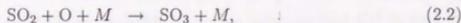
In this study we investigate the effect of the meridional circulation on the distributions of the clouds and condensable gases on Venus. A steady state distribution is numerically solved using a two-dimensional (latitude and height) model. The processes, which alter the distributions, are briefly reviewed in Sections 2.2 and 2.3. The description of the model is given in Section 2.4. The calculated results, discussions and conclusions are given in Sections 2.5 and 2.6.

## 2.2 Chemical processes

The Venus mesosphere (60–90 km) is the region where the solar ultraviolet radiation is mostly absorbed. The photolysis of  $\text{CO}_2$  occurs by absorption of photons with wavelengths shortward of 204 nm,



The production of CO above the cloud is supported by the evidence of an increase of CO mixing ratio with height from 20–30 ppm (ppm =  $\mu\text{mol/mol} = 10^{-6}$ ) below 50 km altitude [Oyama *et al.*, 1980] to  $\sim 50$  ppm above 50 km altitude [Young, 1972]. A major loss of O leads to the formation of  $\text{O}_2$  via the reactions  $\text{O} + \text{O} + M$ ,  $\text{O} + \text{ClO}$  and  $\text{O} + \text{OH}$ , according to Yung and DeMore [1982]. In their one-dimensional models, which account for the observations of mesospheric CO,  $\text{O}_2$  and  $\text{SO}_2$ , the resulting  $\text{O}_2$  is transported downward to the cloud top level by eddy diffusion. The O-O bond is broken by the reactions such as  $\text{S} + \text{O}_2$  [Winick and Stewart, 1980],  $\text{SO} + \text{HO}_2$ ,  $\text{NO} + \text{HO}_2$  and  $\text{ClCO} + \text{O}_2$ . These reactions and the photolyses of  $\text{SO}_2$  and SO constitute catalytic cycles to break  $\text{O}_2$  into O near the cloud top. The O atoms can oxidize  $\text{SO}_2$  at  $\sim 62$  km altitude,



and  $\text{SO}_3$  is rapidly transformed to  $\text{H}_2\text{SO}_4$ ,

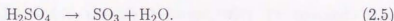


The net of (2.2) and (2.3) can be represented as



*Yung and DeMore* [1982] and *Krasnopolsky and Parshchv* [1981, 1983] have shown that the  $\text{H}_2\text{SO}_4$  formation occurs in a thin layer with a thickness of a few km centered at  $\sim 62$  km altitude.

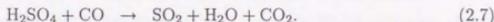
$\text{H}_2\text{SO}_4$  and  $\text{H}_2\text{O}$  condense into cloud particles ( $\text{H}_2\text{SO}_4$ - $\text{H}_2\text{O}$  droplets), which are transported downward by sedimentation, meridional circulation and eddy diffusion. The particles evaporate in the hot lower atmosphere, and then  $\text{H}_2\text{SO}_4$  vapor is thermally decomposed into  $\text{SO}_3$  and  $\text{H}_2\text{O}$ ,



Radio occultation measurements have revealed that  $\text{H}_2\text{SO}_4$  mixing ratio drops precipitously below 38 km altitude, implying that  $\text{H}_2\text{SO}_4$  is decomposed below this height [*Jenkins et al.*, 1994].  $\text{SO}_3$  is expected to be transformed to  $\text{SO}_2$  through the reaction [*Prinn*, 1978; *von Zahn et al.*, 1983]



The net decomposition of  $\text{H}_2\text{SO}_4$  due to (2.5) and (2.6) can be represented as



## 2.3 Transport processes

### 2.3.1 Meridional circulation

The observed mesospheric temperatures are up to 60 K warmer in the polar region and 10 K cooler in the equatorial region than radiative equilibrium temperatures [*Crisp*, 1989]. Such a temperature distribution implies a global-scale meridional circulation with large-scale ascent at low latitudes and descent at high latitudes [*Taylor et al.*, 1983]. The near-infrared spectrometric measurement from the Galileo spacecraft showed that CO mixing ratio increases by  $\sim 35\%$  north of  $47^\circ\text{N}$  at 30–50 km altitudes, implying that CO formed by

the photolysis of  $\text{CO}_2$  above the cloud is transported downward by the descending branch of the meridional circulation at high-latitudes [Collard *et al.*, 1993]. Poleward circulation is traced at  $\sim 65$  km altitude from UV cloud images [Del Genio and Rossow, 1990] and at  $\sim 50$  km altitude from near-infrared cloud images [Belton *et al.*, 1991; Carlson *et al.*, 1991], thus the altitude level of the return flow is lower than  $\sim 50$  km. It should be emphasized that the solar heating within the cloud layer does not necessarily cause a direct cell confined within the cloud layer, because the altitudes of poleward and equatorward flows are determined by the distribution of the Eliassen-Palm flux divergence by atmospheric waves [Haynes *et al.*, 1991] rather than that of solar heating. Imamura [1997] discussed the role of Rossby waves in driving the Venus atmospheric circulation.

The poleward speed at the cloud top is derived from cloud motions to be  $2\text{--}5\text{ m s}^{-1}$  which gives the advective exchange time of 10–100 d [Del Genio and Rossow, 1990], although the derived speed may include tidal components [Neuman and Leovy, 1992]. The deviation of observed temperatures from radiative equilibrium [Crisp, 1989] is consistent with the advective exchange time of  $\sim 90$  d at  $\sim 65$  km altitude [Imamura, 1997]. The strikingly large deviation from radiative equilibrium near the pole [Crisp, 1989] implies that the descent speed in the polar region will be faster than the ascent speed in the equatorial region.

### 2.3.2 Particle sedimentation

The Pioneer Venus particle size spectrometer observed the size distribution to be trimodal with characteristic radii of  $<0.3\ \mu\text{m}$ ,  $1.15\ \mu\text{m}$  and  $3.65\ \mu\text{m}$ , respectively, for the Modes 1, 2 and 3 [Knollenberg and Hunten, 1980]. The Mode 2 particles are the major component of the upper cloud (above  $\sim 57$  km altitude) by weight, while the Mode 3 particles are the major component of the middle ( $50\text{--}57$  km altitudes) and lower ( $46\text{--}50$  km altitudes) clouds by weight. The Mode 2 particles are identified as  $\text{H}_2\text{SO}_4\text{--H}_2\text{O}$  droplets by polarimetric [Young, 1973; Hansen and Hovenier, 1974; Kawabata *et al.*, 1980] and spectrometric [Reed *et al.*, 1978; Pollack *et al.*, 1978] measurements, whereas the composition of the Mode 3 particles remains open to question. Knollenberg and Hunten [1980] believed the Mode 3 particles to be crystalline species, but Toon *et al.* [1984] and Knollenberg [1984] reexamined the data to suggest that the Mode 3 particles can be spherical  $\text{H}_2\text{SO}_4\text{--H}_2\text{O}$  droplets [see also Esposito *et al.*, 1983].

In the present study both Modes 2 and 3 are assumed to be  $\text{H}_2\text{SO}_4\text{--H}_2\text{O}$  droplets. The

droplets are assumed to fall at the Stokes velocity

$$W_{\text{sed}} = \frac{2g\rho r^2}{9\eta}, \quad (2.8)$$

where  $g \sim 8.7 \text{ m s}^{-2}$  is the gravity acceleration,  $\rho \sim 1.8 \times 10^3 \text{ kg m}^{-3}$  is the particle mass density,  $r$  is the particle radius, and  $\eta \sim 1.5 \times 10^{-5} \text{ kg m}^{-1} \text{ s}^{-1}$  is the viscosity of  $\text{CO}_2$  gas. Then the sedimentation speeds for the characteristic radii of Modes 2 and 3 are calculated to be  $W_{\text{sed}} \sim 3 \times 10^{-4} \text{ m s}^{-1}$  and  $3 \times 10^{-3} \text{ m s}^{-1}$ , respectively, leading to the sedimentation time of  $H/W_{\text{sed}} \sim 200 \text{ d}$  above 57 km altitude and  $\sim 25 \text{ d}$  below 57 km altitude, where  $H$  is the atmospheric scale height.

### 2.3.3 Eddy diffusion

The vertical eddy diffusion coefficient  $K_{zz}$  has been estimated to be  $\sim 4 \text{ m}^2 \text{ s}^{-1}$  at 60 km altitude [Woo and Ishimaru, 1981] and  $\sim 0.2 \text{ m}^2 \text{ s}^{-1}$  at 45 km altitude [Woo et al., 1982] from radio scintillation measurements. The time constant of vertical diffusion is  $H^2/K_{zz} \sim 100 \text{ d}$  at 60 km altitude and  $\sim 3700 \text{ d}$  at 45 km altitude.

Convective activity was observed at  $\sim 54 \text{ km}$  altitude in the middle cloud region by the VEGA balloon experiment [Blamont et al., 1986]. This is consistent with the low static stability observed at 51–56 km altitudes, which will be due to infrared heating from below [Schubert et al., 1980]. The upper limit of the vertical diffusion coefficient for the convective transport is estimated as below. The turbulent heat flux  $F$  in this altitude region is given as

$$F = -\rho R K_h \left[ \frac{dT}{dz} + \Gamma \right], \quad (2.9)$$

where  $\rho = 1.0 \text{ kg m}^{-3}$  is the atmospheric density at  $\sim 54 \text{ km}$  altitude,  $R = 191.4 \text{ J kg}^{-1} \text{ K}^{-1}$  is gas constant,  $K_h$  is the diffusion coefficient for heat,  $T$  is temperature,  $z$  is altitude and  $\Gamma$  is adiabatic lapse rate. The static stability is typically as low as  $dT/dz + \Gamma \sim -0.3 \text{ K km}^{-1}$  in this region according to the observations by the Pioneer Venus probes [Seiff et al., 1980; Seiff et al., 1985]. When  $F$  is set equal to the globally-averaged net solar flux of  $\sim 35 \text{ W m}^{-2}$  at 54 km altitude [Tomasko, 1983],  $K_h$  is calculated to be  $\sim 600 \text{ m}^2 \text{ s}^{-1}$  with (2.9). Since the net upward infrared flux calculated from the observed atmospheric structure [Crisp, 1989] is similar to the net downward solar flux in the middle cloud region, the above  $F$  and  $K_h$  values are the upper limits. The value of  $K_{zz}$  will be comparable to that of  $K_h$ .

Mixing in the horizontal direction will be caused by planetary-scale eddies that were observed by cloud trackings [Travis, 1978; Rossow *et al.*, 1990]. However, the effectiveness of the mixing is unknown.

## 2.4 Model descriptions

### 2.4.1 Atmospheric structure, boundary condition and initial condition

A model is run to converge to obtain a steady state solution for the distributions of  $\text{H}_2\text{SO}_4$  and  $\text{H}_2\text{O}$  in a hemisphere with a top height at 70 km and a bottom height at 35 km. The latitudinal resolution is  $2^\circ$  and the vertical resolution is 35–400 m depending on altitude, with the maximum resolution of 35 m around the cloud base so that it may accurately calculate the transport across the cloud base where the cloud density changes rapidly with height. The atmospheric temperature and density profiles are taken from the Venus International Reference Atmosphere [Seiff *et al.*, 1985].

The boundary conditions at the upper, low-latitude ( $0^\circ$ ) and high-latitude ( $90^\circ$ ) boundaries are the absence of the mixing ratio gradients perpendicular to the boundaries. The lower boundary condition for  $\text{H}_2\text{SO}_4$  is the absence of the mixing ratio gradient. The  $\text{H}_2\text{O}$  mixing ratio at the lower boundary is fixed at 30 ppm to be consistent with recent observations [Kamp *et al.*, 1988; Bézard *et al.*, 1990; Crisp *et al.*, 1991; Donahue and Hodges, 1992; Drossart *et al.*, 1993; Meadows and Crisp, 1996; Ignatiev *et al.*, 1997].

The initial distributions of  $\text{H}_2\text{SO}_4$  and  $\text{H}_2\text{O}$  are the constant mixing ratios of 0 ppm and 30 ppm, respectively, for the small- $K_{zz}$  model described later in Section 2.4.3. The initial condition for the large- $K_{zz}$  model is the converged state of the small- $K_{zz}$  model.

### 2.4.2 Production and decomposition of $\text{H}_2\text{SO}_4$ vapor

The production and decomposition processes of  $\text{H}_2\text{SO}_4$  described in Section 2.2 are incorporated into the model in a simplified form. The net  $\text{H}_2\text{SO}_4$  production (2.4) is assumed to occur in a thin layer around 62 km altitude after the one-dimensional photochemical model results by Yung and DeMore [1982] and Krasnopolsky and Parshev [1981, 1983], who estimated the column-integrated production rate of  $\text{H}_2\text{SO}_4$ ,  $\Phi_{\text{H}_2\text{SO}_4} = 10^{12}\text{--}10^{13} \text{ cm}^{-2} \text{ s}^{-1}$ . Considering the dependence of photochemical processes on solar zenith angle,  $\Phi_{\text{H}_2\text{SO}_4}$  is given in the model as  $\Phi_{\text{H}_2\text{SO}_4} = 3.5 \times 10^{12} \cos \phi \text{ (cm}^{-2} \text{ s}^{-1}\text{)}$ , where  $\phi$  is latitude. The vertical

distribution of the production rate is given by a Gaussian probability function centered at 62 km altitude with a half width at half maximum of 1.5 km.

H<sub>2</sub>SO<sub>4</sub> is assumed to be decomposed through the reaction (2.7), and its decomposition rate is given as follows. Assuming the thermochemical equilibrium between (2.3) and (2.5), the decomposition rate of H<sub>2</sub>SO<sub>4</sub> is equal to the loss rate of SO<sub>3</sub> through (2.6),  $L_{\text{SO}_3}$ , as

$$\begin{aligned} L_{\text{H}_2\text{SO}_4} &= L_{\text{SO}_3} \\ &= k_6 [\text{SO}_3][\text{CO}], \end{aligned} \quad (2.10)$$

where  $k_6$  is the rate coefficient for (2.6), and [SO<sub>3</sub>] and [CO] are the number densities of SO<sub>3</sub> and CO, respectively. The SO<sub>3</sub> density is calculated from the densities of H<sub>2</sub>SO<sub>4</sub> and H<sub>2</sub>O using the equilibrium constant between (2.3) and (2.5) [Barin, 1989] after Krasnopolsky and Pollack [1994]. The CO density is given in the model in such a way that it increases with latitude from ~30 ppm at  $\phi < 35^\circ$  to ~40 ppm at  $\phi > 60^\circ$  after the observation by Collard *et al.* [1993]. Since  $k_6$  has not been measured, the value of  $k_6 = 6 \times 10^{-23} \text{ cm}^3 \text{ s}^{-1}$  is adopted so that the model H<sub>2</sub>SO<sub>4</sub> vapor profile at high latitudes may agree with the radio occultation results at 65°N by Jenkins *et al.* [1994] and Kolodner and Steffes [1996].

Note that the association reaction (2.3) should be much faster than the reaction (2.6) so that the equilibrium between (2.3) and (2.5) may be valid. Adopting the expression by Lovejoy *et al.* [1996] for the SO<sub>3</sub> loss through (2.3) as recommended by DeMore *et al.* [1997], the SO<sub>3</sub> loss through (2.3) is more than 3 orders of magnitude greater than that through (2.6) with  $k_6 = 6 \times 10^{-23} \text{ cm}^3 \text{ s}^{-1}$ . Therefore, the adopted  $k_6$  value is consistent with the equilibrium between (2.3) and (2.5).

## 2.4.3 Transport processes

### Meridional circulation

The poleward and upward velocities ( $\bar{v}$ ,  $\bar{w}$ ) associated with the meridional circulation are given as

$$\bar{v} = -\frac{1}{\rho \cos \phi} \frac{\partial \Psi}{\partial z}, \quad (2.11)$$

$$\bar{w} = \frac{1}{\rho a \cos \phi} \frac{\partial \Psi}{\partial \phi}, \quad (2.12)$$

where  $\Psi$  is the mass stream function and  $a$  is the planetary radius. The adopted  $\Psi$  and  $\bar{w}$  are shown in Figure 2.1.  $\bar{v}$  has a maximum of 2 m s<sup>-1</sup> at  $\phi = 48^\circ$  and  $z = 65$  km and the

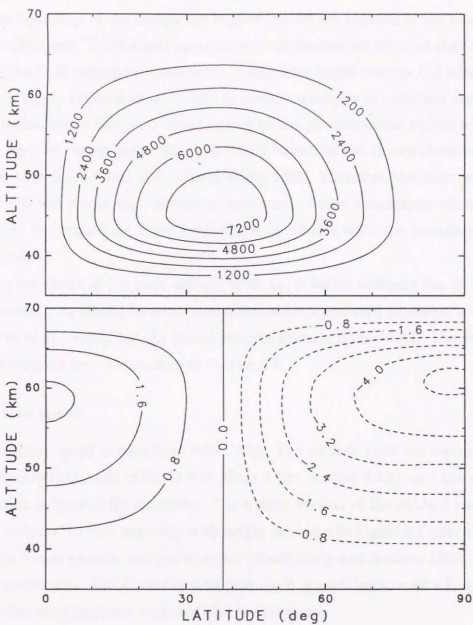


Figure 2.1: (*upper panel*) Mass stream function  $\Psi$  and (*lower panel*) vertical velocity  $\bar{w}$  of the meridional circulation used in the model.  $\Psi$  is in units of  $\text{kg m}^{-1} \text{s}^{-1}$ , while  $\bar{w}$  is in units of  $10^{-3} \text{ m s}^{-1}$ . Above circulation structure is basically consistent with observations (see text).

minimum of  $-0.4 \text{ m s}^{-1}$  at  $\phi=48^\circ$  and  $z=41 \text{ km}$ . The velocities adopted here are basically consistent with the observations described in Section 2.3.1.

The lower boundary of the circulation is placed at 35 km altitude in the model after trace gas distributions. Earth-based spectrometric measurements revealed that at 30–40 km altitudes the COS mixing ratio decreases steeply with height and the CO mixing ratio increases with height [Pollack *et al.*, 1993]. If vertical transport is inefficient around 30–40 km, the region above this level would belong to the photochemical regime where CO is abundant and the region below this level would belong to the thermochemical regime where COS is abundant [Prinn, 1978; Krasnopolsky, 1986]. Therefore, the observed profiles of COS and CO will imply that the above mentioned middle atmospheric circulation is separated from the underlying lower atmospheric circulation with the boundary around 30–40 km altitudes.

Note that the choice of the peak altitude of  $\Psi$ ,  $z_\psi$ , is rather arbitrary ( $z_\psi = 45 \text{ km}$  in the present model).  $z_\psi$  should be lower than 50 km since a poleward advection is observed there [Carlson *et al.*, 1991], but the lowest possible altitude is uncertain. The validity of the  $z_\psi$  value adopted here is examined in Section 2.6.

### Sedimentation speed

The sedimentation speed is calculated with (2.8). The particle radii are assumed to be either the characteristic radii of Mode 2 or Mode 3 (see Section 2.3.2), and the spread of size distribution is ignored for simplicity. The weight fraction of the Mode 3 particles in the cloud is assumed to vary smoothly with height as shown in Figure 2.2 after the result of the Pioneer Venus particle size spectrometer [Knollenberg and Hunten, 1980], and it is fixed in the model run. The dependence on latitude is ignored because of a lack of data. The mean sedimentation speed is plotted also in this figure.

### Diffusion coefficient

The vertical eddy diffusion coefficients  $K_{zz}$  for the "small- $K_{zz}$ " and "large- $K_{zz}$ " models are given as functions of altitude shown in Figure 2.3 after the observations described in Section 2.3.3. The large- $K_{zz}$  model takes account of the convective mixing at 51–56 km altitudes, while the small- $K_{zz}$  model does not. The coefficient in the middle cloud region for the large- $K_{zz}$  model is smaller than the upper limit evaluated in Section 2.3.3.

The horizontal diffusion coefficient  $K_{yy}$  cannot be evaluated from available data. The value of  $K_{yy} = 5 \times 10^5 \text{ m}^2 \text{ s}^{-1}$  is adopted tentatively, after the coefficient of  $10^5$ – $10^6 \text{ m}^2 \text{ s}^{-1}$

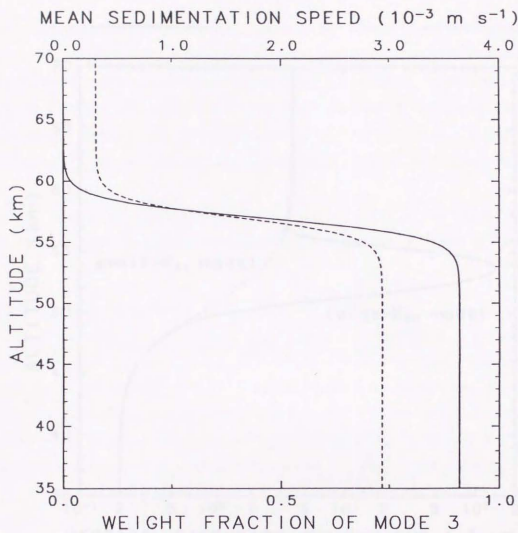


Figure 2.2: Fraction of Mode 3 particles by weight in the cloud (solid curve) adopted in the model after the observation by the Pioneer Venus particle size spectrometer, and the calculated mean sedimentation speed (dotted curve). The cloud mass is assumed to be distributed to Mode 2 ( $r = 1.15 \mu\text{m}$ ) and Mode 3 ( $r = 3.65 \mu\text{m}$ ).

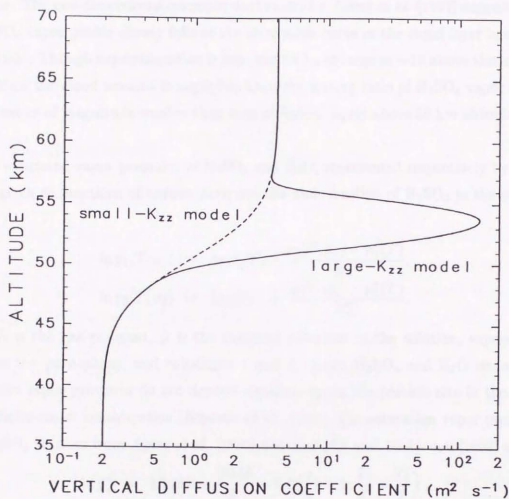


Figure 2.3: Vertical eddy diffusion coefficients  $K_{zz}$  used in the models. Dotted curve is for the "small- $K_{zz}$ " model, while solid curve is for the "large- $K_{zz}$ " model which takes account of the enhanced mixing by convection in the middle cloud region.

for the two-dimensional model of the terrestrial stratosphere [e.g., *Shia et al.*, 1989; *Yang et al.*, 1990].

#### 2.4.4 Condensation and evaporation of H<sub>2</sub>SO<sub>4</sub> and H<sub>2</sub>O

The vapor pressures of H<sub>2</sub>SO<sub>4</sub> and H<sub>2</sub>O are assumed to be limited by their saturated vapor pressures. The one-dimensional microphysical model by *James et al.* [1997] suggested that the H<sub>2</sub>SO<sub>4</sub> vapor profile closely follows the saturation curve in the cloud layer below ~55 km altitude. Though supersaturation is expected to be as large as ~10 above this altitude, its effect on the cloud amount is negligible since the mixing ratio of H<sub>2</sub>SO<sub>4</sub> vapor is more than 3 orders of magnitude smaller than that of H<sub>2</sub>SO<sub>4</sub> liquid above 55 km altitude in the model.

The saturated vapor pressures of H<sub>2</sub>SO<sub>4</sub> and H<sub>2</sub>O, represented respectively by  $p_1$  and  $p_2$ , are given as functions of temperature and the mole fraction of H<sub>2</sub>SO<sub>4</sub> in the solution,  $x_1$ :

$$\ln p_1(T, x_1) = \ln p_1^{\circ}(T) + \frac{\mu_1(T, x_1) - \mu_1^{\circ}(T)}{RT}, \quad (2.13)$$

$$\ln p_2(T, x_1) = \ln p_2^{\circ}(T) + \frac{\mu_2(T, x_1) - \mu_2^{\circ}(T)}{RT}, \quad (2.14)$$

where  $R$  is the gas constant,  $\mu$  is the chemical potential in the solution, superscript  $\circ$  indicates the pure phase, and subscripts 1 and 2 denote H<sub>2</sub>SO<sub>4</sub> and H<sub>2</sub>O respectively. Saturation vapor pressures do not depend significantly on the particle size in the case of the particles under consideration [*Esposito et al.*, 1983]. The saturation vapor pressure of pure H<sub>2</sub>SO<sub>4</sub> is taken from *Ayers et al.* [1980] and *Kulmala and Laaksonen* [1990] as

$$\ln p_1^{\circ} = 16.259 - \frac{10156}{T} + 7.42 \left( 1 + \ln \frac{T_0}{T} - \frac{T_0}{T} \right), \quad (2.15)$$

where  $p_1^{\circ}$  is in units of bar and  $T_0 = 385$  K. The saturation vapor pressure of pure H<sub>2</sub>O is given by *Eisenberg and Kauzmann* [1969] as

$$\ln p_2^{\circ} = \alpha - \frac{\beta}{T} + \frac{\gamma\xi}{T + 0.01} [\exp(\delta\xi^2) - 1] - \epsilon \exp(-\eta\zeta), \quad (2.16)$$

where  $p_2^{\circ}$  is in units of Pa,  $T$  is in units of K,  $\xi = (T + 0.01)^2 - 293700$ ,  $\zeta = (647.26 - T)^{5/4}$ ,  $\alpha = 24.021415$ ,  $\beta = 4616.9134$ ,  $\gamma = 3.1934553 \times 10^{-4}$ ,  $\delta = 2.7550431 \times 10^{-11}$ ,  $\epsilon = 1.0131374 \times 10^{-2}$ , and  $\eta = 1.3158813 \times 10^{-2}$ . The chemical potential  $\mu - \mu^{\circ}$  is given by *Zeleznik* [1991].

Letting the number densities of H<sub>2</sub>SO<sub>4</sub> and H<sub>2</sub>O (including both gaseous and liquid phases) to be  $\rho_1$  and  $\rho_2$ , respectively, and the number density of molecules that exist in

the solution to be  $\rho_{sol}$ , following relations hold:

$$\rho_1 = \frac{p_1}{kT} + x_1 \rho_{sol}, \quad (2.17)$$

$$\rho_2 = \frac{p_2}{kT} + (1 - x_1) \rho_{sol}, \quad (2.18)$$

where  $k$  is the Boltzmann's constant.  $\rho_1$  and  $\rho_2$  are given in the model run as a result of chemical and transport processes, and  $T$  is taken from the assumed atmospheric structure. Then, one can calculate  $p_1$ ,  $p_2$ ,  $\rho_{sol}$  and  $x_1$  with (2.13), (2.14), (2.17) and (2.18). Condensation does not occur when the above equations do not have a solution within the range  $\rho_{sol} > 0$  and  $0 \leq x_1 \leq 1$ .

## 2.5 Model results

### 2.5.1 Cloud structure

The calculated structure in the large- $K_{zz}$  model is shown in Figure 2.4 and Figure 2.5. At low latitudes ( $\phi < 30^\circ$ ), the three-layered structure is evident, being consistent with observations [e.g., *Esposito et al.*, 1983]. The upper cloud is caused by the photochemical production of  $H_2SO_4$  vapor. The middle cloud is caused by the condensation of  $H_2SO_4$  vapor transported upward from below by enhanced eddy mixing at 51–56 km altitudes (see Figure 2.3). Since the middle cloud is absent in the small- $K_{zz}$  model as shown in Figure 2.6, the condensational origin of the middle cloud is confirmed. A similar conclusion was obtained also by *James et al.* [1997] with a one-dimensional model. The lower cloud is caused by the condensation of  $H_2SO_4$  vapor carried aloft by the meridional circulation. The locations of the middle cloud and the cloud base roughly agree with observations, and the calculated peak densities of the upper, middle and lower clouds in the equatorial region are comparable to the observations [*Knollenberg and Hunten*, 1980].

In the upper cloud region, the mass loading increases with latitude (see Figure 2.4) though the photochemical production of  $H_2SO_4$  decreases with latitude. This accumulation is due to the particle transport by the meridional circulation. The cloud top level is relatively low near the pole because of the downward transport by the descending branch of the circulation. The nature of the meridional circulation may be constrained by the observed distribution of the clouds in the upper cloud layer.

The mass loading at high latitudes below ~55 km altitude is enhanced by the transport of cloud particles from the upper and middle cloud regions. The enhanced cloud density

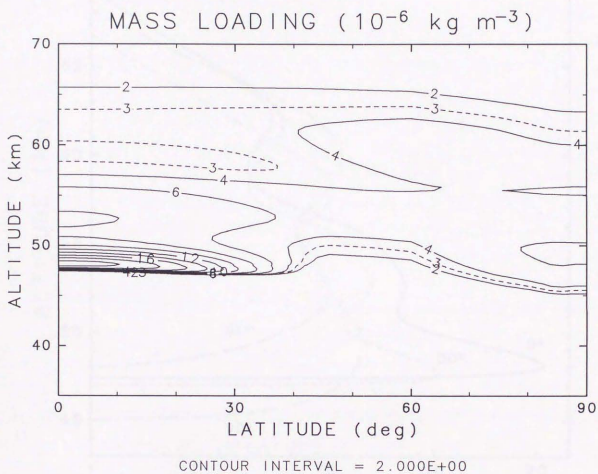


Figure 2.4: Mass loading of  $\text{H}_2\text{SO}_4\text{-H}_2\text{O}$  droplets (in units of  $10^{-6} \text{ kg m}^{-3}$ ) calculated by the large- $K_{12}$  model.

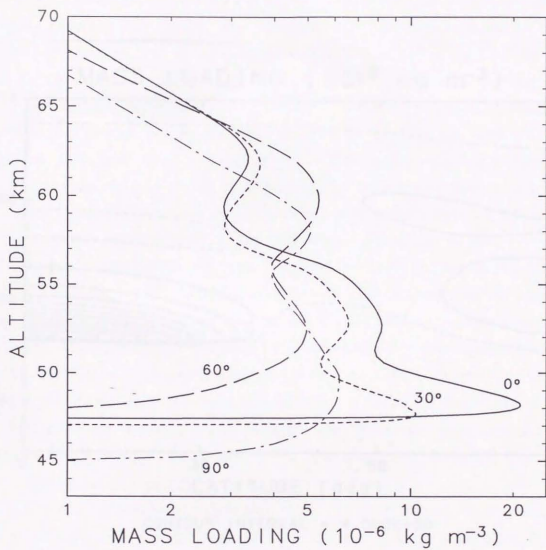


Figure 2.5: Mass loading of  $\text{H}_2\text{SO}_4\text{-H}_2\text{O}$  droplets at  $0^\circ$  (solid),  $30^\circ$  (dotted),  $60^\circ$  (dashed) and  $90^\circ$  (dot-dashed) latitudes in the large- $K_{zz}$  model.

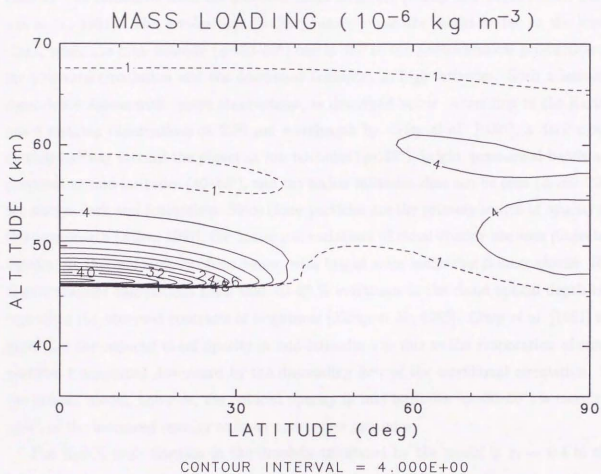


Figure 2.6: Same as Figure 2.4, but for the small- $K_{22}$  model.

and the low temperature at high latitudes lower the cloud base compared with those at mid-latitudes.

Figure 2.7 shows the optical thickness of the cloud at  $2.36 \mu\text{m}$  wavelength, which was calculated from the model result with the Mie scattering theory. The particles were assumed to be either the Mode 2 or Mode 3 (see Figure 2.2) and the spread of size distribution around the mean radii was ignored. The calculated optical thickness is comparable to the value of  $\sim 40$  estimated from the observed cloud structure [Kamp and Taylor, 1990; Carlson et al., 1991]. The low-latitude ( $\phi < 30^\circ$ ) maximum in the model is due to the lower cloud, while the high-latitude ( $\phi = 60\text{--}80^\circ$ ) one is due to the photochemical production in the poleward circulation and the downward transport at high latitudes. Such a latitude dependence agrees with recent observations, as described below. According to the Earth-based imaging observations at  $2.36 \mu\text{m}$  wavelength by Crisp et al. [1991], a dark cloud extends halfway around the planet at low latitudes ( $\phi < 40^\circ$ ), bright quasi-zonal bands are prevalent at mid-latitudes ( $40\text{--}60^\circ$ ), and the higher latitudes that can be seen ( $\phi = 60\text{--}70^\circ$ ) are always dark and featureless. Since cloud particles are the primary source of opacity at this wavelength [Allen, 1987], the horizontal variations of cloud opacity are seen projected against the thermal emission from below, with bright areas indicating thinner clouds. Radiative transfer calculations show that 10–25 % variations in the cloud optical depth can reproduce the observed contrasts of brightness [Kamp et al., 1988]. Crisp et al. [1991] argued that the reduced cloud opacity in mid-latitudes was due to the evaporation of cloud particles transported downward by the descending flow of the meridional circulation. In the present model, however, the reduced opacity in mid-latitudes ( $\phi = 30\text{--}60^\circ$ ) is merely a result of the increased opacity at lower and higher latitudes.

The  $\text{H}_2\text{SO}_4$  mole fraction in the droplets calculated by the model is  $x_1 \sim 0.4$  in the upper cloud region and  $x_1 \sim 0.9$  in the lower cloud region. Remote observations showed that the  $\text{H}_2\text{SO}_4$  concentration in the cloud particles near the cloud top is 75–85% by weight [Young, 1973; Hansen and Hovenier, 1974; Kawabata et al., 1980; Reed et al., 1978; Pollack et al., 1978], corresponding to  $x_1 = 0.35\text{--}0.5$ ; therefore, the model result agrees with the observations. Similar results were obtained also by Krasnopolsky and Pollack [1994] with one-dimensional models.

### 2.5.2 $\text{H}_2\text{SO}_4$ vapor

The  $\text{H}_2\text{SO}_4$  vapor distribution in Figure 2.8 exhibits decrease of mixing ratio below  $\sim 40$  km altitude due to thermal decomposition. The bottom level of the  $\text{H}_2\text{SO}_4$  vapor layer is

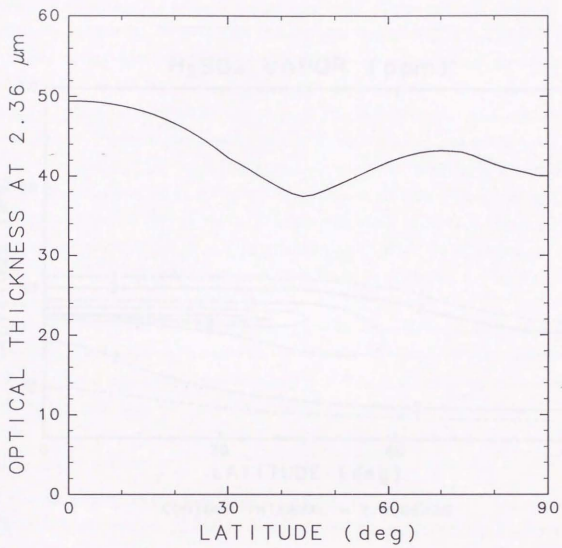


Figure 2.7: Optical thickness of the cloud at 2.36  $\mu\text{m}$  wavelength in the large- $K_{zz}$  model.

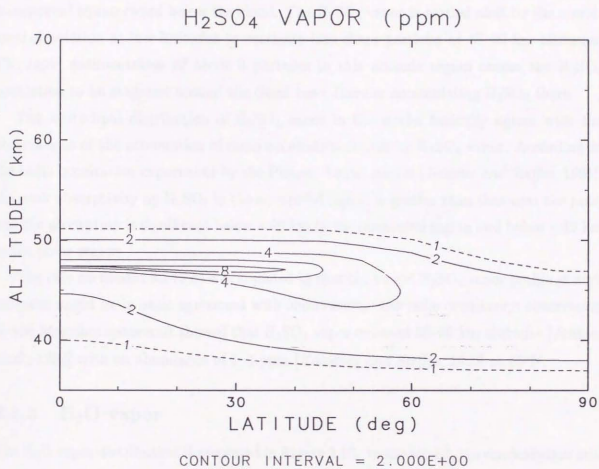


Figure 2.8:  $\text{H}_2\text{SO}_4$  vapor mixing ratio (in units of ppm) calculated by the large- $K_{zz}$  model.

elevated by ascending air at low latitudes, and the mixing ratio is relatively large at low latitudes.

The mechanism of the  $\text{H}_2\text{SO}_4$  accumulation at low latitudes is schematically explained in Figure 2.9. The  $\text{H}_2\text{SO}_4$ - $\text{H}_2\text{O}$  droplets produced near the cloud top are transported poleward and downward by meridional circulation, sedimentation and eddy diffusion. The droplets evaporate in the hot lower atmosphere to yield  $\text{H}_2\text{SO}_4$  vapor, a portion of which is transported equatorward below the cloud. The  $\text{H}_2\text{SO}_4$  vapor is carried aloft by the meridional circulation at low latitudes to condense into cloud particles at 47–50 km altitudes. The rapid sedimentation of Mode 3 particles in this altitude region causes the  $\text{H}_2\text{SO}_4$  circulation to be stagnant around the cloud base, thereby accumulating  $\text{H}_2\text{SO}_4$  there.

The latitudinal distribution of  $\text{H}_2\text{SO}_4$  vapor in the model basically agrees with the observations of the attenuation of radio occultation signals by  $\text{H}_2\text{SO}_4$  vapor. According to the radio occultation experiment by the Pioneer Venus orbiter [Jenkins and Steffes, 1991], the peak absorptivity by  $\text{H}_2\text{SO}_4$  in the equatorial region is greater than that near the pole, and the absorption is significant below ~49 km in the equatorial region and below ~45 km in the polar region.

The rate coefficient for (2.6) was adjusted so that the model  $\text{H}_2\text{SO}_4$  vapor profile at high latitudes might be in basic agreement with observations: the radio occultation observation by the Magellan spacecraft showed that  $\text{H}_2\text{SO}_4$  vapor exists at 38–50 km altitudes [Jenkins et al., 1994] with an abundance of 1–3 ppm [Kolodner and Steffes, 1996] at 65°N.

### 2.5.3 $\text{H}_2\text{O}$ vapor

The  $\text{H}_2\text{O}$  vapor distribution is presented in Figure 2.10. In the model, the condensation into  $\text{H}_2\text{SO}_4$ - $\text{H}_2\text{O}$  droplets causes the density decrease above 55 km altitude, and the downward intrusion of dry air whose water content was reduced through the  $\text{H}_2\text{SO}_4$  production (2.4) causes the density decrease at high latitudes below the cloud.

The model mixing ratio above 60 km altitude is within the observed range of 1–30 ppm derived from Earth-based spectrometric measurements [Fink et al., 1972; Barker, 1975; Encrenaz et al., 1995] and the mass spectrometric measurement on the Pioneer Venus probe [Donahue and Hodges, 1992], although the spectrometric measurement from the Pioneer Venus orbiter revealed a great variability [Schofield et al., 1982]. The model abundance below the cloud is consistent with observations because of the lower boundary value (see Section 2.4.1).

Earth-based spectrometric measurements have not found any latitude dependence of the

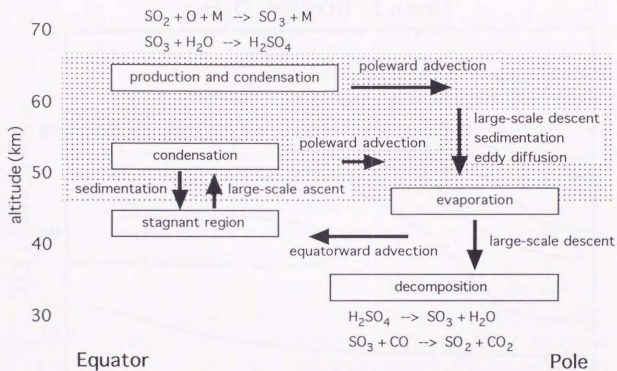


Figure 2.9: Schematic view of the circulation of  $H_2SO_4$  in the Venus atmosphere. Arrows indicate the direction of  $H_2SO_4$  transport. Shaded areas indicate the cloud layer.

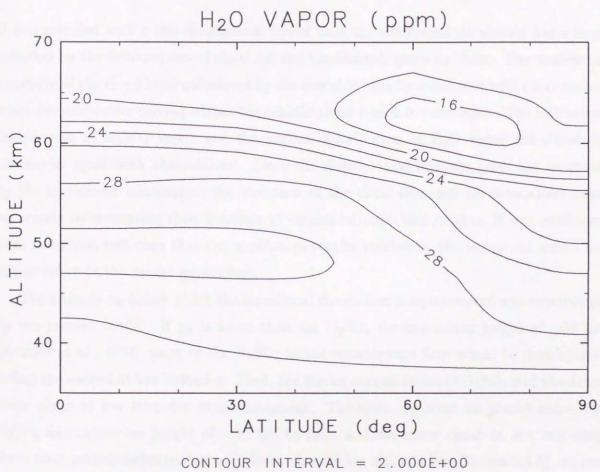


Figure 2.10: H<sub>2</sub>O vapor mixing ratio (in units of ppm) calculated by the large- $K_{z2}$  model.

mixing ratio below the cloud at  $\phi < 60\text{--}70^\circ$  [Bell *et al.*, 1991; Crisp *et al.*, 1991], while the infrared flux measurements by the Pioneer Venus probes suggested a significant decrease of the mixing ratio with latitude at  $\phi < 60^\circ$  [Revercomb *et al.*, 1985]. The relatively uniform distribution of  $\text{H}_2\text{O}$  for  $\phi < 60^\circ$  calculated by the model is consistent with the Earth-based observations.

## 2.6 Discussions and Conclusions

It was revealed with a two-dimensional model that the meridional circulation has a large influence on the distributions of the cloud and condensable gases on Venus. The meridional structure of the cloud layer calculated by the model is broadly consistent with observations when the convective mixing within the middle cloud region is considered. The latitudinal distribution of  $\text{H}_2\text{SO}_4$  vapor and the vertical distribution of  $\text{H}_2\text{O}$  vapor calculated by the model agree with observations. Since the distributions of these gases are governed by the meridional circulation, the structure of the circulation will be determined more accurately by measuring their densities at various latitudes and heights. It was confirmed with numerous test runs that the qualitative results yielded by the numerical model are not sensitive to the model parameters.

The altitude  $z_\psi$  below which the meridional circulation is equatorward was constrained by the present model. If  $z_\psi$  is lower than the  $\text{H}_2\text{SO}_4$  decomposition height of  $\sim 38$  km [Jenkins *et al.*, 1994], most of the  $\text{H}_2\text{SO}_4$  in the equatorward flow would be decomposed before the ascent at low latitudes. Then, the strong accumulation of  $\text{H}_2\text{SO}_4$  and the dense lower cloud at low latitudes would disappear. Therefore,  $z_\psi$  must be placed above the  $\text{H}_2\text{SO}_4$  decomposition height of  $\sim 38$  km to form a dense lower cloud at low latitudes. Since observations indicate that  $z_\psi$  is lower than 50 km altitude (see Section 2.4.3), we can limit  $z_\psi$  in a rather narrow range of 38–50 km.  $z_\psi = 45$  km adopted in the model would be reasonable.

In the present study the size distribution was not solved consistently in the model run. The next step would be to construct a two-dimensional microphysical model which calculates the size development with the method of James *et al.* [1997]. It is expected that the large-scale ascent in the equatorial region will suspend small particles, thereby allowing the particles to coagulate into large particles before the removal by sedimentation.

It is interesting to compare the Venus cloud with the terrestrial stratospheric aerosols whose major composition is  $\text{H}_2\text{SO}_4\text{--H}_2\text{O}$  solution. The life cycle of stratospheric aerosols



## Chapter 3

# Momentum balance of the Venus mid-latitude mesosphere

### 3.1 Introduction

In the Venus mesosphere (60–90 km) the polar regions are warmer than the tropics [Schubert *et al.*, 1980]. The observed mesospheric temperatures are up to 60 K warmer in the polar region and 10 K cooler in the equatorial region than radiative equilibrium temperatures [Crisp, 1989]. Such a temperature distribution implies a global-scale meridional circulation with large-scale ascent at low latitudes and descent at high latitudes [Taylor *et al.*, 1983]. The near-infrared spectrometric measurement from the Galileo spacecraft showed that CO mixing ratio increases by ~35% north of 47°N at 30–50 km altitudes, implying that CO formed by the photolysis of CO<sub>2</sub> above the cloud is transported downward by the descending branch of the meridional circulation at high-latitudes [Collard *et al.*, 1993]. The poleward circulation is traced at ~65 km altitude from UV cloud images [Del Genio and Rossow, 1990] and at ~50 km altitude from near-infrared cloud images [Belton *et al.*, 1991; Carlson *et al.*, 1991]. If such a circulation exists, the conservation of angular momentum at each latitude requires deceleration/acceleration acting on the zonal flow in the poleward/equatorward advection.

Baker and Leovy [1987] have introduced zonal forces into their numerical model in the form of Rayleigh friction, and reproduced subsidence and compressional heating in polar regions. The diagnostic analysis by Hou and Goody [1989] suggests that momentum sources occur at mid-latitudes, since the air moves horizontally across the mid-latitude where angular momentum changes abruptly. Eddy diffusivity cannot transport momentum

enough to maintain the momentum balance except in the turbulent layer in the middle cloud region (51–56 km), as shown later. The semidiurnal tides, which may be important for the maintenance of the superrotation [Fels and Lindzen, 1974; Newman and Leovy, 1992], have little influence on the mean zonal flow at middle and high latitudes [Baker and Leovy, 1987; Hou *et al.*, 1990]. Other mechanisms transferring momentum at mid-latitudes are required. This study shows that the candidates are an upward propagating Rossby wave and internal gravity waves, which are expected to exist in the Venus mesosphere.

In the present study I roughly estimate the forces acting on the zonal flow above clouds by applying the downward control principle [Haynes and McIntyre, 1987; McIntyre, 1989; Haynes *et al.*, 1991], thereby examining the contributions of Rossby and gravity waves in transferring momentum to drive the circulation. The possibility that a Rossby wave controls the variation of the intensity of mid-latitude jets is also discussed.

### 3.2 Zonal force requirement

We consider a steady and zonally averaged atmosphere and use the transformed Eulerian-mean (TEM) equations [Andrews and McIntyre, 1978]. Combining the zonal momentum equation with the mass continuity equation and requiring that  $\rho_0 \bar{w}^* \rightarrow 0$  as  $z \rightarrow \infty$ , we have

$$\rho_0 \bar{w}^* = -\frac{1}{a \cos \phi} \frac{\partial}{\partial \phi} \left[ \cos \phi \int_z^\infty \frac{\rho_0}{\eta} \left( \bar{G} - \frac{\partial \bar{u}}{\partial z} \bar{w}^* \right) dz' \right], \quad (3.1)$$

where

$$\eta = 2\Omega \sin \phi - \frac{1}{a \cos \phi} \frac{\partial(\bar{u} \cos \phi)}{\partial \phi} \quad (3.2)$$

is the absolute vorticity,  $z$  is the log-pressure height,  $\phi$  is the latitude,  $\bar{u}$  is the zonal velocity (eastward is positive),  $\bar{w}^*$  is the vertical component of the residual circulation,  $\rho_0$  is the density proportional to  $\exp(-z/H)$ ,  $H$  is the mean density scale height,  $\Omega$  is the planetary rotation rate,  $a$  is the planetary radius and  $\bar{G}$  is the zonal force per unit mass due to Rossby and gravity wave dissipations and other dissipative eddy processes. Equation (3.1) is similar to the equation (2.6) of Haynes *et al.* [1991] and shows the downward control of the vertical mass flux by zonal forces [Haynes and McIntyre, 1987; McIntyre, 1989]. The downward control nature is evident in the results of the diagnostic analysis by Hou and Goody [1989], although they have not mentioned the principle explicitly.

Here we replace  $\eta(\phi, z')$  in the integral with  $\eta(\phi, z_c)$ , where  $z_c$  is the cloud top level. The replacement is valid insofar as the zonal force is confined to the altitude region where

the zonal wind does not differ significantly from the cloud top wind. Such a condition is satisfied for the Eliassen-Palm (EP) flux divergences by the Rossby and gravity waves discussed in later sections, because the waves are confined below the critical levels where the wind speed is equal to their horizontal phase speeds of 65–70 m s<sup>-1</sup>. The maximum error of the required force (see below) arising from the replacement is an overestimation of ~30%.

Allowing that  $\bar{G} = 0$  and  $\partial\bar{u}/\partial z = 0$  at  $\phi = \pi/2$ , we have the zonal forces vertically integrated above clouds,  $\mathcal{G}$ :

$$\begin{aligned}\mathcal{G} &\equiv \int_{z_c}^{\infty} \rho_0 \bar{G} dz' \\ &\simeq \frac{\eta \rho_0 a}{\cos \phi} \int_{\phi}^{\pi/2} \bar{w}^* \cos \phi' d\phi' + \int_{z_c}^{\infty} \rho_0 \frac{\partial \bar{u}}{\partial z} \bar{w}^* dz',\end{aligned}\quad (3.3)$$

where  $\bar{w}^*$  is related to the departure of temperature from radiative equilibrium,  $\delta\bar{T}$ , as

$$\bar{w}^* \simeq -\frac{\alpha R}{N^2 H} \delta\bar{T},\quad (3.4)$$

where  $N$  is the buoyancy frequency,  $\alpha$  is the radiative relaxation rate and  $R$  is the gas constant. Given the meridional distributions of  $\bar{u}$  and  $\delta\bar{T}$ , (3.3) and (3.4) enable us to calculate  $\mathcal{G}$ .

The distribution of  $\bar{u}$  above clouds has been derived from temperature measurements assuming cyclostrophic balance by *Seiff et al.* [1980] and *Newman et al.* [1984], but their winds derived at the cloud top level (~65 km altitude) are larger than the cloud-tracked winds [*Rossow et al.*, 1980]. Rough estimates using  $\bar{u}$  given by Newman et al. have shown that the neglect of the second term on the right-hand side of (3.3) does not change the latitudinal distribution of  $\mathcal{G}$  significantly (less than 0.01 N m<sup>-2</sup>). For these reasons we consider only the first term on the right-hand side of (3.3), then  $\mathcal{G}$  is calculated using the values at the cloud top level only.  $\delta\bar{T}$  and  $\alpha$  are given by *Crisp* [1989], and other atmospheric parameters are taken from *Seiff et al.* [1985] and *Schubert and Walterscheid* [1984].

Figure 3.1 shows the latitudinal distributions of  $\bar{u}$  and  $\delta\bar{T}$  used for the calculation and the calculated  $\mathcal{G}$  for  $z_c = 65$  km. The distribution of  $\bar{u}$  roughly represents the cloud-tracked winds, and that of  $\delta\bar{T}$  satisfies the equation

$$\int_0^{\pi/2} \delta\bar{T} \cos \phi d\phi = 0\quad (3.5)$$

so that the net vertical mass flux across the cloud top level equals zero.  $\mathcal{G}$  has its maximum in the mid-latitude as a result of the horizontal motions across the mid-latitude

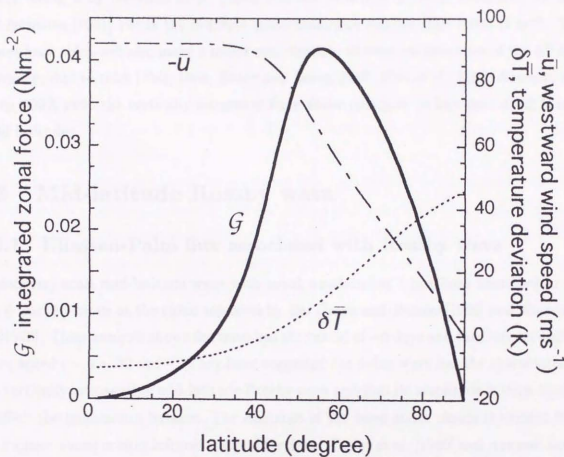


Figure 3.1: Latitudinal distributions of westward wind speed  $-\bar{u}$  (dot-dashed curve) and the departure of temperature from radiative equilibrium  $\delta\bar{T}$  (dotted curve) at the cloud top level used for the calculation, and the calculated zonal force  $\mathcal{G}$  vertically integrated above clouds (bold solid curve).

where angular momentum changes abruptly; this is qualitatively consistent with *Hou and Goody* [1989]. The magnitude of  $\mathcal{G}$  at mid-latitudes is  $0.02\text{--}0.04\text{ N m}^{-2}$ . The mechanisms responsible for the forces must satisfy both the mid-latitude localization and the estimated magnitude. The candidates are a mid-latitude Rossby wave and internal gravity waves, which are expected to transfer momentum upward from the cloud level to the mesosphere. The vertical momentum diffusion by turbulence will make a minor contribution above clouds: using  $\bar{u}$  by *Newman et al.* [1984] and the turbulent diffusion coefficient by *Woo and Ishimaru* [1981] yields the diffusive momentum flux smaller than  $0.005\text{ N m}^{-2}$ . The atmospheric tides will also make a minor contribution: theoretical estimates of the EP flux divergence due to tides [*Fels*, 1986; *Baker and Leovy*, 1987; *Hou et al.*, 1990; *Newman and Leovy*, 1992] yield the vertically integrated force above clouds to be less than  $0.005\text{ N m}^{-2}$  at all latitudes.

### 3.3 Mid-latitude Rossby wave

#### 3.3.1 Eliassen-Palm flux associated with Rossby wave

A planetary-scale mid-latitude wave with zonal wavenumber 1 has been identified in the cloud-tracked winds at the cloud top level by *Del Genio and Rossow* [1990] and *Rossow et al.* [1990]. Their analysis shows the wave has the period of  $\sim 5$  days and the Doppler-shifted phase speed  $c - \bar{u} \sim 32\text{ m s}^{-1}$ . They have suggested the 5-day wave has the characteristics of a vertically propagating mid-latitude Rossby wave and that its amplitude is large enough to affect the momentum balance. The existence of the wave above clouds is evident from the Pioneer Venus orbiter infrared radiometer data: *Taylor et al.* [1980] and *Apt and Leung* [1982] report 5.5-day and 5.3-day periodicities, respectively, in the mid-latitude brightness temperature. *Taylor et al.* [1980] suggested the vertical propagation of the wave with a vertical phase velocity of the order  $4 \times 10^{-2}\text{ m s}^{-1}$ . The decrease of the amplitude from the cloud top to the 80-km altitude [*Apt and Leung*, 1982] implies the EP flux divergence at 65–80 km altitudes.

The source of the 5-day wave is unclear. Barotropic instability of the zonal flow is a likely mechanism for producing eddies. The analysis of UV images suggests the occurrence of barotropic eddy disturbances at mid-latitudes [*Travis*, 1978]. In the mature stage of the disturbance a nonlinear cascade of energy to larger eddies will produce a Rossby wave having a zonal wavenumber 1 [*Rossow and Williams*, 1979]. A portion of the required zonal force may be attributed to the equatorward momentum transport by barotropic eddies,

which might be important for the maintenance of the superrotation [Gierasch, 1975].

Now we roughly estimate the EP flux associated with the Rossby wave at the cloud top level using a linear theory on a mid-latitude  $\beta$ -plane [e.g., Andrews *et al.*, 1987]. The vertical component of the EP flux,  $F$ , is given by

$$F \simeq \frac{1}{2} \rho_0 \epsilon k m |\hat{\Psi}|^2, \quad (3.6)$$

where

$$m \simeq \left[ \frac{\beta}{\epsilon(\bar{u} - c)} - \frac{k^2}{\epsilon} - \frac{1}{4H^2} \right]^{\frac{1}{2}} \quad (3.7)$$

is the vertical wavenumber,  $\epsilon = f_0^2/N^2$ ,  $f_0 = 2\Omega^* \sin \phi_0$  is the Coriolis parameter at latitude  $\phi_0$ ,  $\Omega^*$  is the angular velocity for a coordinate system rotating with the local wind at  $\phi_0$ ,  $k = (a \cos \phi_0)^{-1}$  is the zonal wavenumber,  $\beta$  is the absolute vorticity gradient and  $\hat{\Psi}$  is the amplitude of stream function.

The key parameter for the  $F$  evaluation is the amplitude of the observed 5-day wave. The zonal wind distribution assumed for the  $\mathcal{G}$  evaluation (see Figure 3.1) is similar to the time-averaged values observed in 1979 and 1985, in which the contrast of mid-latitude jets was decreased [Rossow *et al.*, 1990]. During those periods the lower limits of the meridional wind amplitude at 20–40° latitudes ranged from 6 to 8 m s<sup>-1</sup> [Rossow *et al.*, 1990]. We adopt tentatively the value of 8 m s<sup>-1</sup> as the typical amplitude at  $\phi_0 = 45^\circ$  where  $\beta$  peaks.

Taking  $\hat{\Psi} = (8 \text{ m s}^{-1})/k$ ,  $c - \bar{u} = 32 \text{ m s}^{-1}$ ,  $\Omega^* = -2\pi(3.47 \text{ day})^{-1}$  and  $\beta = -10^{-11} \text{ m}^{-1} \text{ s}^{-1}$  at  $\phi_0 = 45^\circ$  [Del Genio and Rossow, 1990], and  $N = 2 \times 10^{-2} \text{ s}^{-1}$  and  $H = 5 \text{ km}$  as characteristic values at mid-latitudes, we obtain the EP flux at the cloud top level to be  $F \sim 0.022 \text{ N m}^{-2}$  with the vertical wavelength of  $\sim 22 \text{ km}$ . The vertical phase speed is estimated to be  $\sim 5 \times 10^{-2} \text{ m s}^{-1}$ , being roughly consistent with the observation [Taylor *et al.*, 1980]. The estimated EP flux  $0.022 \text{ N m}^{-2}$  is the same order of magnitude as the required forces at mid-latitudes, 0.02–0.04 N m<sup>-2</sup> (see Figure 3.1). Therefore, the mid-latitude Rossby wave contributes significantly to the driving of the meridional circulation.

### 3.3.2 Suppression of mid-latitude jets by the wave-driven circulation

Pioneer Venus ultraviolet images, which covers five 80-day periods in 1979–1985, revealed the vacillation of the cloud top dynamics with a time scale of several years [Del Genio and Rossow, 1990; Rossow *et al.*, 1990], as described below. An equatorial 4-day wave and a mid-latitude 5-day wave are present in both the brightness and cloud-tracked wind data.

The 4-day wave, which has long been observed as the so-called "Y" feature, is identified as a Kelvin wave with a wavenumber of unity and an intrinsic phase speed of  $\sim 6 \text{ m s}^{-1}$ . The 5-day wave is identified as a Rossby wave as mentioned before. The amplitudes of the Kelvin and Rossby waves vary with time: both of the waves were intense in 1979 and 1985 (*active state*) and weak in 1980–1982 (*quiescent state*). The mean zonal winds given by Rossow *et al.* [1990] are plotted in Figure 3.2. During the quiescent state the equatorial zonal wind was 5–10  $\text{m s}^{-1}$  smaller than other periods. The contrast of mid-latitude jets gradually increased from 1979 to 1983 and decreased (tentatively) from 1983 to 1985.

The meridional circulation transports heat poleward to drive the middle atmosphere away from the radiative equilibrium [Taylor, 1983], thereby weakening the jets whose contrasts are determined by the poleward temperature gradient through cyclostrophic balance [Schubert, 1983]. Since the Rossby wave drives a meridional circulation to transport heat poleward, the development/decay of Rossby wave weakens/intensifies the jets. This is qualitatively consistent with the observation: the development of mid-latitude jets in 1980–1982 coincides with the decay of the Rossby wave [Rossow *et al.*, 1990]. This hypothesis is examined quantitatively below using the observations at the cloud top. In order for the wave-driven circulation to suppress the jet, the latitudinal temperature contrast across the jet,  $\Delta T$ , must be within the same order of magnitude as the temperature change induced by the wave-driven circulation,  $\delta T$ .

From cyclostrophic balance, the latitudinal temperature contrast  $\Delta T$  associated with the jet is roughly estimated from

$$2U \frac{\Delta U}{\Delta z} \sim \frac{R}{H \tan \phi_J} \frac{\Delta T}{\Delta \phi}, \quad (3.8)$$

where  $U$  is the typical zonal wind speed,  $\Delta U$  is the contrast of the jet,  $\Delta z$  is the vertical scale of the shear beneath the jet,  $R = 191.4 \text{ J kg}^{-1} \text{ K}^{-1}$  is the gas constant,  $H$  is the scale height,  $\phi_J$  is the latitude of the jet, and  $\Delta \phi$  is the width of the jet. From the UV images [Del Genio and Rossow, 1990; Rossow *et al.*, 1990], we assume that  $U = 90 \text{ m s}^{-1}$ ,  $\Delta U = 10\text{--}20 \text{ m s}^{-1}$ ,  $\phi_J = 45^\circ$  and  $\Delta \phi = 30^\circ$ .  $\Delta z$  allows large uncertainty, then  $\Delta z \sim H$ . With above parameters, we obtain  $\Delta T \sim 5\text{--}10 \text{ K}$  at the cloud top.

The wave-driven circulation reduces the temperature contrast between high and low latitudes. The decrease of the temperature contrast,  $\delta T$ , is estimated from the thermodynamic relation

$$W_{\text{high}} - W_{\text{low}} \sim \frac{\alpha R}{N^2 H} \delta T. \quad (3.9)$$

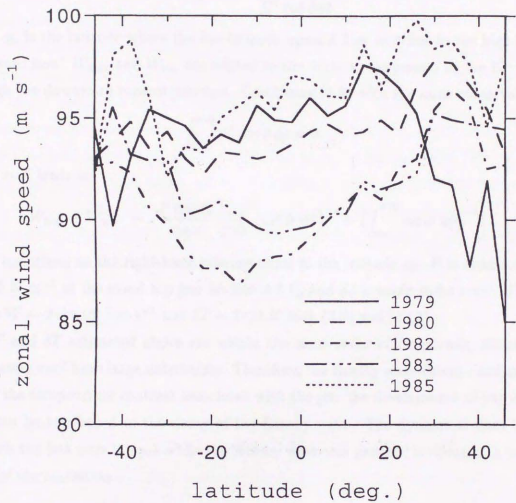


Figure 3.2: Mean zonal wind speeds at the cloud top observed from the Pioneer Venus orbiter during five imaging periods from 1979–1985. Data are given by Rossow *et al.* [1990]. The wind speeds of  $\sim 90 \text{ m s}^{-1}$  near the equator are referred to as the superrotation.

$W_{\text{high}}$  and  $W_{\text{low}}$  are the typical values of vertical speed  $\bar{w}^*$  at high and low latitudes, respectively, associated with the wave-driven circulation:

$$\begin{aligned} W_{\text{high}} &\equiv \frac{\int_{\phi_0}^{\pi/2} \bar{w}^* \cos \phi d\phi}{\int_{\phi_0}^{\pi/2} \cos \phi d\phi}, \\ W_{\text{low}} &\equiv \frac{\int_0^{\phi_0} \bar{w}^* \cos \phi d\phi}{\int_0^{\phi_0} \cos \phi d\phi}, \end{aligned} \quad (3.10)$$

where  $\phi_0$  is the latitude where the low-latitude upward flow switches to the high-latitude downward flow.  $W_{\text{high}}$  and  $W_{\text{low}}$  are related to the vertical component of the EP flux,  $F$ , through the downward control principle. Combining (3.3) with the mass conservation

$$\int_0^{\pi/2} \bar{w}^* \cos \phi d\phi = 0 \quad (3.11)$$

and  $\mathcal{G} = \mathcal{F}$  leads to

$$W_{\text{high}} - W_{\text{low}} \sim \frac{F \cos \phi_0}{\eta \rho_0 a} \left[ \left( \int_0^{\phi_0} \cos \phi d\phi \right)^{-1} + \left( \int_{\phi_0}^{\pi/2} \cos \phi d\phi \right)^{-1} \right], \quad (3.12)$$

where quantities on the right-hand side are those at the latitude  $\phi_0$ .  $F$  is estimated to be  $\sim 0.022 \text{ N m}^{-2}$  at the cloud top [see Section 3.3.1], and  $\phi_0$  is taken to be  $\sim 45^\circ$ . Then, we obtain  $W \sim 2\text{--}3 \times 10^{-3} \text{ m s}^{-1}$  and  $\delta T \sim 7\text{--}11 \text{ K}$  with (3.9) and (3.12).

$\Delta T$  and  $\delta T$  estimated above are within the same order of magnitude, although the parameters used have large uncertainty. Therefore, the Rossby wave-driven circulation can cancel the temperature contrast associated with the jet: the development of jets in 1980–1982 can be attributed to the decay of the Rossby wave. The dynamical state in 1983, in which the jets were intense while the Rossby wave was present, is thought to be in the midst of the transition.

### 3.4 Internal gravity waves

Small-scale wavelike structures have been observed in the Venus atmosphere [Rossow *et al.*, 1980; Blamont *et al.*, 1986; Seiff and Kirk, 1991; Hinson and Jenkins, 1995], and some of them may be attributed to internal gravity waves. Their latitudinal distributions are, however, highly uncertain.

The activity of gravity waves generated by convection at the ground surface [Hou and Farrell, 1987] is unlikely to localize in the mid-latitude since observations show greater penetration of sunlight at smaller solar zenith angle [Tomasko, 1983]. The distribution of the waves generated by the convection in the middle cloud region is uncertain since

the convective activity depends on the heat transport in the lower atmosphere [Leroy and Ingersoll, 1996].

The gravity waves generated by topography [Young *et al.*, 1994] can be responsible for the zonal forces in the mid-latitude. The near-surface direct cell transports westward momentum downward at mid- and high latitudes, thereby producing westward surface winds there. At low latitudes, on the other hand, the advection from higher latitudes produces eastward surface winds. Since the waves generated by eastward surface winds have critical levels near the surface, the momentum transport by topographically-generated waves will localize in the mid-latitude. The momentum transport by such waves cannot be evaluated because of the uncertainty in the surface wind distribution.

Generation of gravity waves by shear (KH) instability in the middle cloud region will also be localized in the mid-latitude where wind shear is relatively large [Imamura, 1997]. Around the middle cloud region, where the atmosphere is close to neutral static stability due to infrared heating from below [Schubert *et al.*, 1980], the Richardson number falls short of 0.25 which is the critical value for the initiation of shear instability. Radar observations have revealed that the excitation sources of short-period gravity waves in the terrestrial stratosphere are located near the jet stream [Murayama *et al.*, 1994], in which unstable shear layers will generate gravity waves [e.g., Sutherland and Peltier, 1994]: it would be reasonable to expect the same mechanism to work on Venus. The momentum transport by such waves in the Venus atmosphere cannot be evaluated with available data.

### 3.5 Conclusions

The characteristic time of advective exchange for parcels in the Venus mesosphere (here we take  $z > 65$  km) is defined as  $\tau_A = \mathcal{M}/\mathcal{F}$ , where  $\mathcal{M}$  is the total mesospheric air mass and  $\mathcal{F}$  is the vertical mass flux across the 65 km altitude surface in the ascent region at lower latitudes. Using the parameters given earlier, the advective exchange time is calculated to be  $\tau_A \sim 90$  d (d = earth days). On the other hand, the characteristic time of vertical diffusion is defined as  $\tau_D = H^2/K_{zz}$ , where  $K_{zz}$  is the vertical eddy diffusion coefficient. Using the value  $K = 4 \text{ m}^2 \text{ s}^{-1}$  at  $\sim 60$  km altitude [Woo and Ishimaru, 1981] yields  $\tau_D \sim 100$  d. Thus advective transport is as important as eddy diffusion for tracer transport.

In this study the forces acting on the zonal flow above clouds have been estimated from the cloud-tracked zonal winds and the departure of temperature from radiative equilibrium at the cloud top level by applying the downward control principle. The EP flux associated

with a Rossby wave is within the same order of magnitude as the required forces; therefore, the major part of the meridional circulation will be driven by the Rossby wave. It was also shown that the variation of the jet intensity with a time scale of several years is consistent with the variation of Rossby wave activity. Gravity waves may account for a portion of the required forces, but their contributions are still uncertain.

The results suggest that the concept of a "wave-driven extratropical pump" [e.g., *Holton et al., 1995*] is valid in the Venus mesosphere as well as in the terrestrial stratosphere (see Figure 3.3), although the Venus mesosphere is in approximate cyclostrophic balance rather than in geostrophic balance. In the terrestrial stratosphere Rossby or gravity waves, which are presumably generated in the troposphere, induce zonal forces on the mean flow. The forces drive a global-scale extratropical fluid-dynamical suction pump which withdraws air upward and poleward from the tropical troposphere and pushes it poleward and downward into the extratropical troposphere.

## Chapter 4

### Heat Transport in the Venus Atmosphere

#### Atmosphere

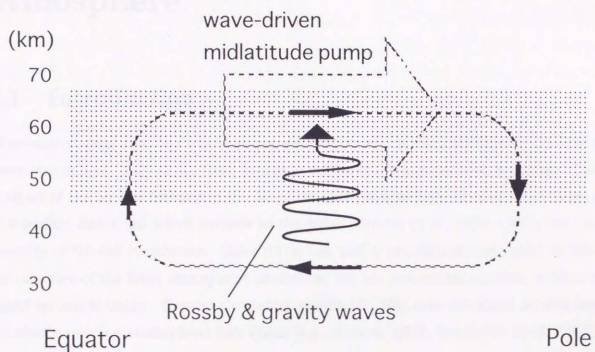


Figure 3.3: Dynamical aspects of the meridional circulation at the Venus cloud level. Angular momentum advection associated with the meridional circulation is canceled by the EP flux divergences associated with Rossby or gravity waves. Small-scale turbulence may also be important around the middle cloud region.

## Chapter 4

# Heat transport in the deep Venus atmosphere

### 4.1 Introduction

Observations show that the temperatures are nearly uniform with latitude in the Venus lower atmosphere [Seiff *et al.*, 1980] probably due to the dynamical heat transport. The analyses of the aeolian features in the Magellan radar images have revealed the existence of a surface direct cell which extends to the poles [Greeley *et al.*, 1992, 1995], but the intensity of the cell is unknown. Stone [1974] has used a two-dimensional model to infer the structure of the lower atmospheric circulation, but the momentum equation in Stone's model ignores rotation. General circulation models (GCMs) were developed to simulate the slowly rotating atmospheres like Venus [e.g., Rossow, 1983; Del Genio *et al.*, 1993], but the radiative relaxation rates assumed in those models are much larger than those in the Venus lower atmosphere. Since the Venus lower atmosphere is characterized by the slow radiative relaxation due to large thermal inertia and large opacity in infrared, the predicted flow speeds in those models cannot be accepted.

The diagnostic analysis by Hou and Goody [1989] shows a shallow direct cell with a meridional flow speed of  $\sim 1 \text{ cm s}^{-1}$  and an overlying shallow reverse cell within a scale height ( $\sim 14 \text{ km}$ ) from the surface. Their results may be, however, incorrect as described below. The streamfunction obtained by Hou and Goody [1989] shows an equatorward residual circulation at the cloud top level ( $\sim 65 \text{ km}$  altitude) and a reverse cell within the main cloud deck, but a poleward circulation is traced at the cloud top from UV cloud images [Del Genio and Rossow, 1990] and near the cloud base from near-infrared cloud images [Belton

*et al.*, 1991; *Carlson et al.*, 1991]. Since the particle streamline trajectories predicted by the mean winds derived from cloud motions are consistent with the orientation of linear cloud features [*Carlson et al.*, 1991], the mean cloud motions will well represent the residual circulation. Therefore, the streamfunction obtained by *Hou and Goody* [1989] conflicts with observations. The streamfunction determined by their method will be sensitive to the error in the temperature distribution, which was determined from a parameterized zonal wind distribution.

In this study the circulation speed is estimated with a new method. A direct cell transports heat poleward only if the poleward branch of the circulation at higher levels is on the average at a higher potential temperature than the equatorward branch at lower levels [*Stone*, 1975]: a stable stratification is indispensable to the poleward heat transport. The net poleward flux of potential temperature, which can be diagnosed from radiative energy balance, is a function of the meridional flow speed and the vertical gradient of potential temperature. Therefore, the typical flow speed can be estimated from the radiative energy balance and the static stability observed. The upward heat transport by the cell and the angular momentum balance are also discussed.

## 4.2 Estimation of circulation speed

### 4.2.1 Potential temperature flux

The thermodynamic equation for a zonally averaged, steady state atmosphere in the transformed Eulerian mean coordinate is [e.g., *Andrews et al.*, 1987]

$$\frac{v}{a} \frac{\partial \theta}{\partial \phi} + w \frac{\partial \theta}{\partial z} = Q, \quad (4.1)$$

where  $v$  and  $w$  are the meridional and vertical velocities of the residual circulation,  $\phi$  is latitude,  $z$  is log-pressure altitude,  $a$  is planetary radius, and  $\theta$  is potential temperature.

The diabatic heating  $Q$  is defined as

$$Q = \left( \frac{\partial F_S}{\partial z} - \frac{\partial F_T}{\partial z} \right) \frac{e^{\kappa z/H}}{\rho c_p}, \quad (4.2)$$

where  $F_S$  is the net downward flux of solar radiation,  $F_T$  is the net upward flux of thermal radiation,  $\kappa = R/c_p$ ,  $R$  is gas constant,  $c_p$  is heat capacity,  $H$  is mean scale height,  $\rho = \rho_s e^{-z/H}$  is the nominal basic state density, and  $\rho_s$  is the density at the surface.

In order to investigate the heat balance at each latitude, (4.1) is integrated over  $z$  from the surface to the top boundary of the cell,  $z_{top}$ . The boundary between the lower atmo-

spheric circulation under consideration and the overlying middle atmospheric circulation is expected to be located at 30–40 km altitudes from COS and CO distributions as discussed in Section 2.4.3. Assuming the vertical mass flux across the level  $z_{top}$  to be small, (4.1) and the continuity equation yield

$$\mathcal{F}(\phi) \approx -(\rho_s \cos \phi)^{-1} \int_{\phi}^{\pi/2} \int_0^{z_{top}} a \cos \phi' \rho Q d\phi' dz, \quad (4.3)$$

where

$$\mathcal{F}(\phi) \equiv \int_0^{z_{top}} v\theta e^{-z/H} dz \quad (4.4)$$

is the poleward potential temperature flux vertically integrated at the latitude  $\phi$ . The  $Q$  distribution near the surface is uncertain since the processes through which the solar energy absorbed by the ground surface is surrendered to the atmosphere are poorly understood. Since  $e^{\kappa z/H} \sim 1$  for small  $z$ , however, the total diabatic heating near the surface below a level  $z_l$  is approximately the net flux across the level  $z_l$ . Then, substituting (4.2) into (4.3), we obtain

$$\begin{aligned} \mathcal{F}(\phi) \approx & -(\rho_s \cos \phi)^{-1} \int_{\phi}^{\pi/2} a \cos \phi' \\ & \times \left[ \frac{(F_S - F_T)_{z=z_l}}{c_p} + \int_{z_l}^{z_{top}} dz \left( \frac{\partial F_S}{\partial z} - \frac{\partial F_T}{\partial z} \right) \frac{e^{\kappa z/H}}{c_p} \right] d\phi'. \end{aligned} \quad (4.5)$$

The level  $z_l$  will be placed at a few kilometers above the surface. Equation (4.5) enables us to calculate  $\mathcal{F}$  from  $F_S$  and  $F_T$ .

Since  $\mathcal{F}$  is a function of  $v$  and  $\theta$  [see (4.4)], the typical meridional speed can be estimated from the  $\mathcal{F}$  value and the  $\theta$  distribution when the circulation structure is specified as follows. The boundary between the poleward and equatorward branches,  $z_b$ , is assumed to be at the level where the pressure is the average of those at  $z = 0$  and  $z_{top}$  so that the flow speeds in the poleward and equatorward branches may be similar. The typical  $\theta$  contrast between the higher and lower levels is  $z_b(d\bar{\theta}/dz)$ , where  $d\bar{\theta}/dz$  is the typical  $\theta$  gradient. Then, from (4.4),  $\mathcal{F}$  is related to the typical meridional speed  $\bar{v}$  as

$$\begin{aligned} \mathcal{F} & \approx \bar{v} \left[ \left( \bar{\theta}_l + \frac{d\bar{\theta}}{dz} z_b \right) \int_{z_b}^{z_{top}} e^{-z/H} dz - \bar{\theta}_l \int_0^{z_b} e^{-z/H} dz \right] \\ & \approx \bar{v} \frac{d\bar{\theta}}{dz} z_b^2, \end{aligned} \quad (4.6)$$

where  $\bar{\theta}_l$  is the typical  $\theta$  at lower levels. The relations  $2e^{-z_b/H} = e^{-z_{top}/H} + 1$  and  $e^{-z_b/H} \approx 1 - z_b/H$  are used in deriving (4.6). Since  $z_b$  may not be at the level specified above in the real Venus atmosphere, (4.6) gives the definition of the "typical meridional speed". Equation (4.6) enables us to estimate  $\bar{v}$  from  $\mathcal{F}$  and  $d\bar{\theta}/dz$ .

### 4.2.2 Solar radiation

With the solar flux model  $F_S^0(z)$  for the subsolar point (cosine of the zenith angle,  $\mu = 1$ ) given by *Hou and Goody* [1989], the solar flux varies as  $F_S^0(z)\mu^{1.4}$ : the exponent is compounded from a geometric factor  $\mu$  and a reflectivity factor  $\mu^{0.4}$  [*Tomasko*, 1983]. This expression for the solar flux agrees with all the measured data within the limits of observations [*Hou and Goody*, 1989]. It is straightforward to show that the zonally averaged flux is expressed as [*Hou and Goody*, 1981]

$$F_S(z, \phi) = 0.285 F_S^0(z) (\cos \phi)^{1.4}. \quad (4.7)$$

$F_S^0(z)$  increases with height from 95 W m<sup>-2</sup> at the ground surface to 160 W m<sup>-2</sup> at 30 km altitude.

### 4.2.3 Thermal radiation

$F_T$  cannot be modeled after thermal flux measurements only, because the measurement of thermal radiation is limited. The thermal flux in the Venus lower atmosphere is written in the opaque limit

$$F_T = -\frac{4}{3\bar{k}_R} \frac{\partial \sigma T^4}{\partial z}, \quad (4.8)$$

where  $\bar{k}_R$  is the Rosseland mean absorption coefficient,  $\sigma$  is the Stefan's constant and  $T$  is temperature.  $\bar{k}_R$  may be calculated theoretically, but far-wing absorptions in high pressures are not well understood, and the coefficient depends on the water mixing ratio which is uncertain [*Pollack et al.*, 1980]. The preferred approach is to determine  $\bar{k}_R$  from solar radiation fluxes as follows.

#### Case I

Case I follows *Hou and Goody* [1989], where  $\bar{k}_R$  is a function of  $z$  only. Assuming that the globally averaged state is close to radiative equilibrium with the average solar flux,  $\bar{k}_R(z)$  is calculated with the relation

$$\bar{F}_S(z) = -\frac{4}{3\bar{k}_R(z)} \frac{\partial \sigma \bar{T}^4}{\partial z}, \quad (4.9)$$

where  $\bar{F}_S(z) = 0.208 F_S^0(z)$  is the global mean solar flux and  $\bar{T}$  is the global mean temperature. Adopting  $\bar{T}$  from *Schubert and Walterscheid* [1984],  $\bar{k}_R(z)$  is calculated to be as shown in Figure 4.1.

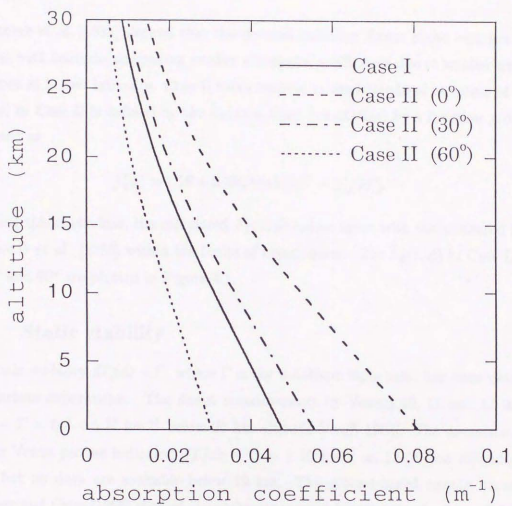


Figure 4.1: Absorption coefficient  $\bar{k}_R$  in Cases I and II. For Case II, the  $\bar{k}_R$  values at the latitudes  $0^\circ$ ,  $30^\circ$  and  $60^\circ$  are plotted.

An upward heat transport by the cell causes the underestimation of  $\bar{k}_R$  when (4.9) is used, thereby shifting the apparent thermal cooling distribution downward within the region of the cell. The error in the  $\mathcal{F}$  evaluation due to such an incorrect cooling distribution is up to  $e^{\alpha z_0/H} - 1 \sim 15\%$  [see (4.2)], which is negligible in the present rough estimates.

## Case II

Revercomb *et al.* [1985] showed that the thermal radiation fluxes above  $\sim 20$  km altitude increase with latitude, suggesting smaller absorption coefficients due to smaller water mixing ratios at higher latitudes. Case II takes account of the latitudinal variation of  $\bar{k}_R$ . The  $\bar{k}_R(z, \phi)$  in Case II is defined by the  $\bar{k}_R(z)$  in Case I multiplied by a function  $f(\phi)$ , which is defined as

$$f(\phi) = 1.16 + 0.582 \tanh[(30^\circ - \phi)/20^\circ]. \quad (4.10)$$

Adopting this coefficient, the calculated  $F_T(z, \phi)$  values agree with the measured fluxes of Revercomb *et al.*, [1985] within the limits of observations. The  $\bar{k}_R(z, \phi)$  in Case II at  $\phi = 0^\circ, 30^\circ$  and  $60^\circ$  are plotted in Figure 4.1.

### 4.2.4 Static stability

The static stability  $dT/dz - \Gamma$ , where  $\Gamma$  is the adiabatic lapse rate, has been determined with various experiments. The direct measurements by Venera 10, 11 and 12 indicated  $dT/dz - \Gamma = 0.3\text{--}0.5$  K km $^{-1}$  below 20 km altitude [Seiff, 1983]. The measurements by Pioneer Venus probes indicated  $dT/dz - \Gamma \sim 1$  K km $^{-1}$  at 12–20 km altitudes [Seiff, 1980], but no data are available below 12 km. The ground-based remote sounding by Meadows and Crisp [1996] showed the nightside averaged lapse rate of  $-7$  to  $-7.5$  K km $^{-1}$  below 6 km, implying  $dT/dz - \Gamma \sim 1$  K km $^{-1}$ . Given these measurements, the value of  $d\bar{\theta}/dz \approx dT/dz - \Gamma = 0.5\text{--}1$  K km $^{-1}$  is adopted in the present study.

### 4.2.5 Result

Figure 4.2 shows an example of a set of  $\mathcal{F}$  distributions that were calculated using (4.5) with  $z_{top} = 30$  km (which gives  $z_0 = 9$  km) and  $z_l = 5$  km. Though  $\mathcal{F}$  peaks at  $\sim 45^\circ$  latitude, the zonally integrated flux peaks at  $\sim 30^\circ$  latitude because the geometric factor  $\cos \phi$  must be multiplied. The greater flux in Case II than in Case I is due to the greater infrared cooling at high latitudes in Case II. Applying (4.6) to these results with  $d\bar{\theta}/dz =$

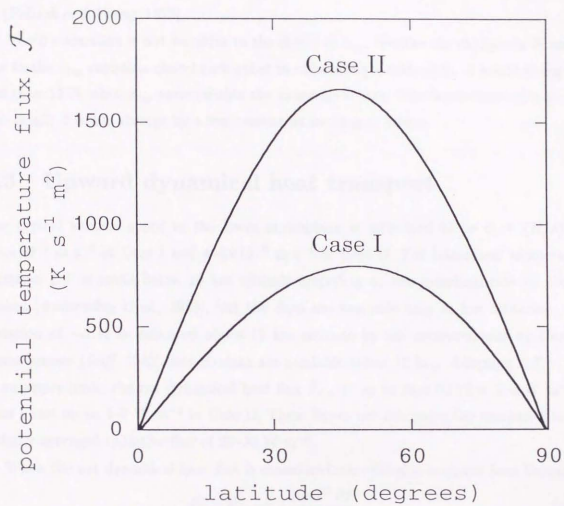


Figure 4.2: Latitudinal distribution of the vertically-integrated poleward flux of potential temperature,  $\mathcal{F}$ , in Cases I and II. The top boundary of the cell is assumed to be at  $z_{top} = 30$  km.

0.5–1 K km<sup>-1</sup>, we obtain  $\bar{v} = 1\text{--}2$  cm s<sup>-1</sup> in Case I and  $\bar{v} = 2\text{--}4$  cm s<sup>-1</sup> in Case II in the mid-latitude. These values are close to the threshold speed for the windblown dust on Venus estimated by *Iversen et al.* [1976]. The advection time scale is calculated to be  $a/\bar{v} = 10\text{--}20$  yr in Case I and 5–10 yr in Case II, that are much longer than the planetary rotation period of 243 days and are comparable to the radiative relaxation time of 20–30 yr [Pollack and Young, 1975].

The  $\bar{v}$  estimation is not sensitive to the choice of  $z_{top}$ , because the changes in  $\mathcal{F}$  and  $z_b$  due to the  $z_{top}$  variation cancel each other in calculating  $\bar{v}$  with (4.6).  $\bar{v}$  would change by less than 15 % when  $z_{top}$  varies within the range 20–40 km. The dependence of  $\bar{v}$  on  $z_l$  is also small:  $\bar{v}$  would change by a few percent as far as  $z_l < 10$  km.

### 4.3 Upward dynamical heat transport

The typical vertical speed in the lower atmosphere is estimated to be  $\bar{w} = (H/a)\bar{v} = 2\text{--}4 \times 10^{-5}$  m s<sup>-1</sup> in Case I and  $4\text{--}8 \times 10^{-5}$  m s<sup>-1</sup> in Case II. The latitudinal temperature variation  $\Delta T$  is small below 10 km altitude according to the measurements by Venera probes [Arduevskiy et al., 1983], but the data are available only at low latitudes. The variation of  $\sim 5$  K is indicated above 12 km altitude by the measurements by Pioneer Venus probes [Seiff, 1983], but no data are available below 12 km. Adopting  $\Delta T \sim 5$  K as an upper limit, the net dynamical heat flux  $\bar{F}_{dyn}$  is up to  $\bar{\rho}c_p\bar{w}\Delta T/2 = 2\text{--}4$  W m<sup>-2</sup> in Case I and up to 4–7 W m<sup>-2</sup> in Case II. These fluxes are not negligible compared to the globally-averaged radiative flux of 20–30 W m<sup>-2</sup>.

When the net dynamical heat flux is considered, the globally-averaged heat balance is

$$\bar{F}_S - \bar{F}_{dyn} = -\frac{16\sigma\bar{T}^3}{3k_R} \frac{\partial \bar{T}}{\partial z}. \quad (4.11)$$

Thus a nonzero  $\bar{F}_{dyn}$  would reduce the temperature lapse rate. Even if the radiative equilibrium state is super-adiabatic as suggested by greenhouse models [e.g., Pollack et al., 1980], the upward heat transport by the cell may cause a stable stratification [Stone, 1974].

### 4.4 Implications for superrotation

As mentioned earlier, the top boundary of the surface direct cell is expected to be located at 30–40 km altitudes from trace gas distributions (see Section 2.4.3). The presence of the top boundary at this height region is consistent with the observed zonal wind profile if the superrotation is maintained by the mechanism of *Gierasch* [1975], who argued

that direct cells transport angular momentum upward. A general circulation model, which involves a surface direct cell and an overlying middle atmospheric (direct) cell, yields a distinct superrotation through the *Gierasch's* mechanism [Del Genio et al., 1993]. When the *Gierasch's* theory is adopted, the absence of the upward transport of angular momentum near the boundary would result in a small wind shear. The observations by the Pioneer Venus probes [Counselman et al., 1980] indicate such a small wind shear around 25–40 km altitudes.

Now we investigate an equilibrium state in which the upward transport of angular momentum by the cell is balanced with the downward transport by eddy viscosity adopting the theory of *Gierasch* [1975]. Assuming that the horizontal eddy viscosity is effective enough to cause a rigid-body rotation of the mean zonal flow, *Gierasch* [1975] obtained the relation

$$\frac{U(z)}{\Omega a} + 1 = \exp \left[ \frac{3}{2\nu_v} \int_0^z dz' \int_0^{\pi/2} d\phi w(z, \phi) \cos^3 \phi \right], \quad (4.12)$$

where  $U$  is the equatorial zonal velocity,  $\Omega$  is the planetary rotation rate and  $\nu_v$  is the vertical eddy viscosity coefficient. The assumption of rigid-body rotation is justified in the lower atmosphere by observations [Schubert, 1983]. Assuming that the low-latitude upward flow switches to the high-latitude downward flow around the 30° latitude where zonally-integrated poleward heat flux peaks (see Section 4.2.5), the integration over  $\phi$  in (4.12) is approximately

$$\begin{aligned} \int_0^{\pi/2} d\phi w \cos^3 \phi &\approx \bar{w} \left( \int_0^{\pi/6} d\phi \cos^3 \phi - \int_{\pi/6}^{\pi/2} d\phi \cos^3 \phi \right) \\ &= \frac{\bar{w}}{4}. \end{aligned} \quad (4.13)$$

Then, (4.12) is rewritten as

$$\nu_v \frac{dU}{dz} \approx \frac{3}{8} \bar{w} (U + \Omega a), \quad (4.14)$$

where the left and right hand sides represent the downward transport of angular momentum by eddy viscosity and the upward transport by the cell, respectively. Around the level  $z_b = 9$  km,  $U$  and  $dU/dz$  are typically  $\sim 7$  m s<sup>-1</sup> and  $\sim 0.0025$  s<sup>-1</sup>, respectively, from the Pioneer Venus Sounder and Venera 12 results that were obtained near the equator [e.g., Schubert, 1983]. Adopting the  $\bar{w}$  values estimated before, (4.14) yields  $\nu_v = 0.03$ – $0.05$  m<sup>2</sup> s<sup>-1</sup> for Case I and  $\nu_v = 0.05$ – $0.1$  m<sup>2</sup> s<sup>-1</sup> for Case II. The diffusion time scale is  $H^2/\nu_v = 100$ – $200$  yr for Case I and  $H^2/\nu_v = 60$ – $100$  yr for Case II, that are much longer than the advection time scale of 5–20 yr. *Matsuda* [1980] argued that the planetary rotation must be faster than

the vertical momentum diffusion in order for a fast superrotation to exist: the estimated  $\nu_v$  value is consistent with *Matsuda's* conclusion.

## 4.5 Conclusions

The intensity of the surface direct cell was inferred from the radiative energy balance at each latitude and the static stability observed. The advection time scale was estimated to be much longer than the planetary rotation period and comparable to the radiative relaxation time. The estimated circulation speed and the observed latitudinal temperature contrast yielded the net upward heat transport by the cell of several  $\text{W m}^{-2}$ , which may have caused the stable stratification observed. It was also suggested that the vertical diffusion time scale is much longer than the advection time scale.

The material transport by the surface direct cell has not been considered in the atmospheric and surface chemistries of Venus, although atmospheric constituents are transported mostly by the cell rather than by eddy diffusion. Since the Venus atmosphere is not at thermochemical equilibrium even in the lowest scale height [*Fegley et al.*, 1997], the chemical reactions in the course of the equatorward circulation will cause latitudinal variations of atmospheric composition and surface material. Observations of such latitudinal contrasts are useful to examine the conclusions obtained in this study.

## Chapter 5

# Radiative damping of gravity waves and turbulence in the upper atmospheres of terrestrial planets

### 5.1 Introduction

The turbulence and mean-wind acceleration caused by gravity waves play important roles in determining the meridional circulation and thermal structure of the Earth's upper atmosphere [e.g., *Garcia and Solomon*, 1985], and a similar mechanism is expected to work in the Venus and Mars upper atmospheres [*Zhang and Bougher*, 1996; *Barnes*, 1990]. The signatures of small-scale atmospheric waves are observed also on Venus [*Murray et al.*, 1974; *Belton et al.*, 1976a,b; *Rosow et al.*, 1980; *Counselman et al.*, 1980; *Ingersoll et al.*, 1987; *Hinson and Jenkins*, 1995] and on Mars [*Nier and McElroy*, 1977; *Seiff and Kirk*, 1977; *Anderson and Leovy*, 1978], but their characteristics are uncertain. The role of gravity waves in the material circulation depends on the dissipation processes: the waves dissipating due to radiative damping or molecular viscosity decelerate the zonal wind to drive the meridional circulation without generating turbulence, while convectively-breaking waves do generate turbulence. Since the composition of thermosphere is sensitive to the altitude of turbopause, atmospheric escape rates depend on the gravity wave activity and the wave dissipation processes. It is necessary to clarify the dissipation processes of gravity waves for the understanding of both short-term and long-term material transports.

The radiative damping of wavelike perturbations with small vertical scales has been studied so far for the Earth's atmosphere [e.g., *Fels*, 1982, 1984; *Apruzese and Strobel*,

1984; *Zhu and Strobel*, 1991; *Zhu*, 1993], but there is no detailed investigation concerning its effect on the amplitude growth with height. Moreover, the radiative damping in the upper atmospheres of other planets has not been investigated except the early work by *Hodges* [1969] where the effect of collisional excitation by atomic oxygen (see later) was ignored. In this study the effect of radiative damping on the amplitude growth of gravity waves is investigated theoretically for the Earth, Venus and Mars upper atmospheres. The radiative damping of wave-induced turbulence is also evaluated for the Mars atmosphere as an assessment.

## 5.2 Radiative damping rate

### 5.2.1 Method

The atmosphere is considered to be homogeneous for typical gravity waves with vertical wavelength less than one scale height, so we may apply the method of *Fels* [1984] according to the formulation by *Spiegel* [1957]. *Fels* developed an analytic solution for the radiative damping rate in non-LTE (local thermodynamic equilibrium) regions as a function of the wavenumber of the imposed harmonic temperature perturbation in an infinite homogeneous medium. The solution is given as:

$$\tau_{LTE}^{-1} \approx \left[ \tau_{LTE} + \frac{1}{2} \tau_{coll} r^{-1} (1 - \gamma^{-1})^{-1} \left( \frac{kT}{\Delta E} \right)^2 \frac{dB}{dT} \exp \left( \frac{kT}{\Delta E} \right) \right]^{-1}, \quad (5.1)$$

where

$$\begin{aligned} \tau_{LTE}^{-1} = & \frac{4\pi}{M_{air} c_p} \frac{dB}{dT} r \sum_i S_i \\ & \times \int d\nu f_i(\nu) \left[ 1 - S_i f_i(\nu) x \tan^{-1} \left( \frac{1}{S_i f_i(\nu) x} \right) \right] \end{aligned} \quad (5.2)$$

is the damping rate in LTE conditions,  $\tau_{coll}$  is the collisional relaxation time,  $r$  is the mixing ratio of the absorber,  $\gamma$  is the ratio of specific heats,  $k$  is the Boltzmann's constant,  $T$  is temperature,  $\Delta E$  is the vibrational energy under consideration,  $B$  is the Planck function,  $M_{air}$  is the mean molecular weight of the air,  $c_p$  is the heat capacity of air,  $S_i$  is the intensity of the  $i$ -th transition,  $f_i(\nu)$  is the line profile,  $x = \rho_n r / m$  is a measure of the absorber amount per unit wavelength,  $\rho_n$  is the atmospheric number density, and  $m$  is the vertical wavenumber of the imposed perturbation. The principal infrared radiation that relaxes thermal perturbations is the  $\text{CO}_2(\nu_2)$  15  $\mu\text{m}$  radiation. We do not consider the  $\text{O}_3$

9.6  $\mu\text{m}$  radiation, although it is not negligible in the Earth's upper stratosphere [e.g., *Fels*, 1982].

In non-LTE regions of upper atmospheres, the collisional excitation of the  $\text{CO}_2(\nu_2)$  mode by atomic oxygen is important [e.g., *Bougher et al.*, 1994]. Atomic oxygen is one of the major constituents in the Mars and Venus upper atmospheres as well as in the Earth's upper atmosphere [*Hanson et al.*, 1977; *McElroy et al.*, 1977; *Hedin et al.*, 1983]. The rate coefficient for the deexcitation of  $\text{CO}_2(\nu_2)$  by atomic oxygen,  $K_{\text{CO}_2-\text{O}}$ , has been reported by several investigators. The recent rocket experiment by *Rodgers et al.* [1992] supports the rate coefficient given by *Sharma and Wintersteiner* [1990],  $K_{\text{CO}_2-\text{O}} = 3.5 \times 10^{-13} \sqrt{T} + 2.32 \times 10^{-9} \exp(-76.75/T^{1/3}) \text{ cm}^3 \text{ s}^{-1}$ , which we adopted. The rate coefficients for the deexcitation by air ( $\text{N}_2$ ,  $\text{O}_2$ ),  $K_{\text{CO}_2-\text{AIR}}$ , and by  $\text{CO}_2$ ,  $K_{\text{CO}_2-\text{CO}_2}$ , were taken from *Allen et al.* [1980] and *Dickinson* [1972], respectively. The line spectral parameters of the  $\text{CO}_2(\nu_2)$  band were taken from the HITRAN database [*Rothman et al.*, 1992].

The Earth's atmospheric model was taken from the U. S. Standard Atmosphere, with the atomic oxygen density from *Llewellyn et al.* [1993]. The Mars atmospheric structure was adopted from *Bougher and Dickinson* [1988] that is compatible with the observations of *Hanson et al.* [1977] and *McElroy et al.* [1977]. The Venus atmospheric structure was taken from *Seiff et al.* [1985] for pressure and temperature. The Venus atmospheric composition is taken from *von Zahn et al.* [1983] and *Hedin et al.* [1983].

## 5.2.2 Result

Figure 5.1 shows the radiative damping rate  $\tau_{\text{NLTE}}^{-1}$  calculated with (5.1) plotted against the vertical wavelength. Calculations were carried out only above 100 km altitude for Venus because of a limited validity of the isolated-line approximation used. The damping rate in the Venus atmosphere is much smaller below  $\sim 80$  km than above  $\sim 100$  km since the 15  $\mu\text{m}$  radiation is trapped locally because of the large optical thickness. The collisional excitation of  $\text{CO}_2(\nu_2)$  by atomic oxygen enhances the 15  $\mu\text{m}$  emission in non-LTE regions. To illustrate this effect, the damping rate for the case neglecting atomic oxygen is shown by dotted curves at 120 km altitude.

The damping rate is much greater in the Mars atmosphere than in the Earth's atmosphere. This is because  $\text{CO}_2$  is the dominant constituent in the Mars atmosphere whereas it is a minor constituent in the Earth's atmosphere. The damping rate is larger in the Mars atmosphere than in the Venus atmosphere at 100 km altitude for typical vertical wavelengths, because radiative damping works more effectively in optically thin regions.

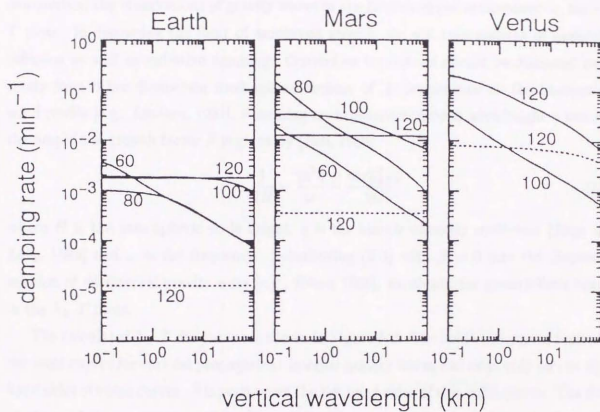


Figure 5.1: Radiative damping rates  $\tau_{NLTE}^{-1}$  in the Earth, Mars and Venus upper atmospheres (solid curves). Dotted curves represent those for the atmospheres without atomic oxygen. Numerals labeled for the curves represent altitudes in km.

The situation is different at 120 km altitude since the deviation from LTE suppresses the CO<sub>2</sub> 15 μm emission in the Mars upper atmosphere.

### 5.3 Limit of amplitude growth

The  $\lambda_H$ - $T$  plots are useful to characterize gravity waves according to their amplitude growth with height, where  $\lambda_H$  is the horizontal wavelength and  $T$  is the period. *Manson* [1990] summarized the observations of gravity waves in the Earth's upper atmosphere on the  $\lambda_H$ - $T$  plots. In discussing the limit of amplitude growth, we will take account of molecular diffusion as well as radiative damping. Convective breakdown should be discussed separately from other dissipation mechanisms because of its dependence on the background wind profile [e.g., *Lindzen*, 1981]. Assuming an exponential growth with height  $z$  like  $e^{\beta z}$ , the amplitude growth factor  $\beta$  is given by [*Fels*, 1982]

$$\beta = \frac{1}{2H} - \frac{m^3 \eta}{\omega} - \frac{m \tau_{NLTE}^{-1}}{2\omega}, \quad (5.3)$$

where  $H$  is the atmospheric scale height,  $\eta$  is the kinetic viscosity coefficient [*Kaye and Laby*, 1986] and  $\omega$  is the frequency. Substituting (5.3) with  $\beta = 0$  into the dispersion relation of an internal gravity wave [e.g., *Hines*, 1960], we obtain the growth limit curves in the  $\lambda_H$ - $T$  plots.

The calculated  $\lambda_H$ - $T$  diagrams are shown in Figure 5.2. The bold solid curves represent the limit curves for vertical propagation: internal gravity waves can exist only on the right hand sides of these curves.  $\beta$  is positive on the left hand sides of thin solid curves. The data of observed waves summarized by *Manson* [1990] mostly scatter in the region of positive  $\beta$ , hence this result will be valid. It can be seen from this figure that radiative damping is more effective than molecular diffusion below 80 km altitude on the Earth, below 120 km altitude on Mars and even above 120 km altitude on Venus for typical gravity waves.

### 5.4 Suppression of turbulence by radiative damping

Radiative damping reduces wave energy, thereby weakening the turbulence caused by the convective breakdown of gravity waves. The effect of radiative damping on wave-induced turbulence is evaluated by considering a gravity wave whose amplitude is saturated [*Lindzen*, 1981] due to wave-induced turbulent diffusion and radiative damping. A case study is performed for the Mars atmosphere at 100 km altitude where molecular diffusion



is unimportant (see Figure 5.2). Considering the wave-induced turbulent diffusion instead of molecular diffusion, (5.3) is rewritten as

$$\beta = \frac{1}{2H} - \frac{m^3 K_{zz}}{\omega} - \frac{m \tau_{NLTE}^{-1}}{2\omega}, \quad (5.4)$$

where  $K_{zz}$  is the turbulent diffusion coefficient. In the absence of the mean wind shear, the amplitude growth factor for a saturated wave is  $\beta = 0$ . Then, from (5.4) and the dispersion relation we get

$$K_{zz} \sim \frac{c^4 k_H}{2HN^3} - \frac{\tau_{NLTE}^{-1}}{2m^2}, \quad (5.5)$$

where  $c$  is the intrinsic horizontal phase speed,  $k_H = 2\pi/\lambda_H$  is the horizontal wavenumber, and  $N$  is the Brunt-Väisälä frequency. The 1st term on the right-hand side of (5.5) represents the turbulent diffusion caused by the breakdown of a gravity wave in the absence of radiative damping, while the 2nd term represents the reduction of turbulent diffusion by radiative damping.

Stationary gravity waves, that will be excited frequently in the Mars lower atmosphere due to its large topography, are expected to propagate to the upper atmosphere to cause turbulence and mean-wind deceleration [Barnes, 1990; Joshi *et al.*, 1995]. For such stationary waves  $c$  is equal to  $-\bar{u}$ , where  $\bar{u}$  is the mean wind. Since the  $\bar{u}$  distribution in the Mars upper atmosphere is uncertain, an example is shown for  $c = -\bar{u} = 20 \text{ m s}^{-1}$  which yields  $\lambda_z = 12 \text{ km}$  from the dispersion relation. Figure 5.3 shows the effect of radiative damping on  $K_{zz}$  calculated with (5.5) for various  $\lambda_H$ . The  $\tau_{NLTE}^{-1}$  value was adopted from Figure 5.1. Radiative damping reduces  $K_{zz}$  by  $\sim 540 \text{ m}^2 \text{ s}^{-1}$  in this case. For moderate waves with  $\lambda_H \sim 100 \text{ km}$ , the Lindzen's [1981] gravity wave parameterization overestimates  $K_{zz}$  significantly when radiative damping is ignored. The results at  $\lambda_H > 125 \text{ km}$  are absurd: turbulence is not generated by such waves because of radiative damping.

## 5.5 Conclusions

The radiative damping of gravity waves in the non-LTE regions of the Earth, Mars and Venus atmospheres have been investigated. It was shown that the radiative damping due to the  $\text{CO}_2$   $15 \mu\text{m}$  radiation limits wave propagation much more effectively in the Mars atmosphere than in the Earth's atmosphere. It was shown that radiative damping is more effective than molecular diffusion below 80 km altitude on the Earth, below 120 km altitude on Mars and even above 120 km altitude on Venus. It was also demonstrated

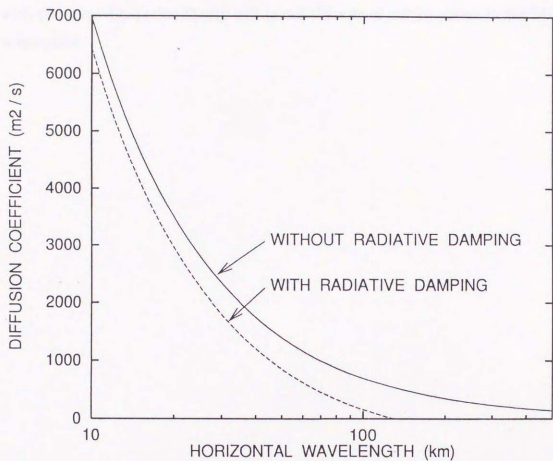


Figure 5.3: Wave-induced turbulent diffusion coefficient  $K_{zz}$  as a function of the horizontal wavelength  $\lambda_H$  with (dashed curve) and without (solid curve) radiative damping, for a gravity wave with  $c = 20 \text{ m s}^{-1}$  in the Mars atmosphere at 100 km altitude.

for the Mars upper atmosphere that turbulent diffusion can be weakened significantly by radiative damping. It is possible that the "turbopause" height is controlled partly by large-scale meridional circulation as well as turbulent diffusion in the upper atmospheres where radiative damping is significant.

It is expected that gravity wave signatures will be observed in the Mars upper atmosphere by the Thermal Plasma Analyzer and the Neutral Mass Spectrometer on board the Planet-B satellite, whose periapsis altitude is as low as 150 km. The analyses of those data with the wave dissipation theory will reveal the role of gravity waves in the Mars upper atmosphere.

## Acknowledgements

The author wishes his appreciation to Profs. T. Ogawa and N. Iwagami for their guidance during the doctoral course, for stimulating discussions and for carefully reading of the manuscript. The author thanks Profs. Y. Matsuda and M. D. Yamanaka, G. L. Hashimoto, M. Fujiwara, and K. Kita for stimulating discussions. The study described in Chapter 2 has been done in collaboration with G. L. Hashimoto. Profs. M. Nakamura and Y. Abe are also appreciated for carefully reading of the manuscript and providing critical comments.

## References

- Allen, D. C., T. Scragg and C. J. S. M. Simpson, Low temperature fluorescence studies of the deactivation of the bend-stretch manifold of CO<sub>2</sub>, *Chem. Phys.*, *51*, 279-298, 1980.
- Allen, D. A., The dark side of Venus, *Icarus*, *69*, 221-229, 1987.
- Andrews, D. G., and M. E. McIntyre, Generalized Eliassen-Palm and Charney-Drazin theorems for waves on axisymmetric mean flows in compressible atmosphere. *J. Atmos. Sci.*, *35*, 175-185, 1978.
- Anderson, E. and C. Leovy, Mariner 9 television limb observations of dust and ice hazes on Mars, *J. Atmos. Sci.*, *35*, 723-734, 1978.
- Andrews, D. G., J. R. Holton, and C. B. Leovy, *Middle Atmosphere Dynamics*, 150 pp., Academic, San Diego, Calif., 1987.
- Apruzese, J. P. and D. F. Strobel, Radiative relaxation rates for individual 15- $\mu$  CO<sub>2</sub> lines in the upper stratosphere and lower mesosphere, *J. Geophys. Res.*, *89*, 7187-7194, 1984.
- Apt, J., and J. Leung, Thermal periodicities in the Venus atmosphere, *Icarus*, *49*, 427-437, 1982.
- Ayers, G. P., R. W. Gillett, and J. L. Gras, On the vapor pressure of sulfuric acid, *Geophys. Res. Lett.*, *7*, 433-436, 1980.
- Avduevskiy, V. S., Structure and parameters of the Venus atmosphere according to Venera probe data, in *Venus*, edited by D. M. Hunten, L. Colin, T. M. Donahue, and V. I. Moroz, pp.280-298, Univ. of Ariz. Press, Tucson, 1983.
- Baker, N. L., and C. B. Leovy, Zonal winds near Venus' cloud top level: A model study of the interaction between the zonal mean circulation and the semidiurnal tide, *Icarus*, *69*, 202-220, 1987.
- Barin, I., *Thermochemical Data of Pure Substances*, VCH, Weinheim, 1989.
- Barker, E. S., Observations of Venus water vapor over the disk of Venus: the 1972-74 data using the H<sub>2</sub>O lines at 8197 Å and 8176 Å, *Icarus*, *25*, 268-281, 1975.

- Barnes, J. R., Possible effects of breaking gravity waves on the circulation of the middle atmosphere of Mars, *J. Geophys. Res.*, *95*, 1401-1421, 1990.
- Belton, M. J. S., G. R. Smith, D. A. Elliott, K. Klaasen and G. E. Danielson, Space-time relationships in the UV markings on Vevus, *J. Atmos. Sci.*, *33*, 1383-1393, 1976a.
- Belton, M. J. S. and G. R. Smith, Cloud patterns, waves and convection in the Venus atmosphere, *J. Atmos. Sci.*, *33*, 1394-1417, 1976b.
- Bézar, B., C. de Bergh, D. Crisp, and J.-P. Maillard, The deep atmosphere of Venus revealed by high-resolution nightside spectra, *Nature*, *345*, 508-511, 1990.
- Bell III, J. F., D. Crisp, P. G., Lucey, T. A. Ozoroski, W. M. Sinton, S. C. Willis, and B. A. Campbell, Spectroscopic observations of bright and dark emission features on the night side of Venus, *Science*, *252*, 1293-1296, 1991.
- Belton, M. S. J. et al., Images from Galileo of the Venus cloud deck, *Science*, *253*, 1531-1536, 1991.
- Blamont, J. E., et al., Implication of the VEGA balloon results for Venus atmospheric dynamics, *Science*, *231*, 1422-1425, 1986.
- Blamont, J. E., R. E. Young, A. Seiff, B. Ragent, R. Sagdeev, V. M. Linkin, V. V. Kerzhanovich, A. P. Ingersoll, D. Crisp, L. S. Elson, R. A. Preston, G. S. Golitsyn, and V. N. Ivanov, Implication of the VEGA balloon results for Venus atmospheric dynamics, *Science*, *231*, 1422-1425, 1986.
- Bougher, S. W. and R. E. Dickinson, Mars mesosphere and thermosphere 1. global mean heat budget and thermal structure, *J. Geophys. Res.*, *93*, 7325-7337, 1988.
- Bougher, S. W., D. M. Hunten and R. G. Roble, CO<sub>2</sub> cooling in the terrestrial planet atmospheres, *J. Geophys. Res.*, *99*, 14609-14622, 1994.
- Brock, C. A., P. Hamill, J. C. Wilson, H. H. Jonsson, and K. R. Chan, Particle formation in the upper tropical troposphere: a source of nuclei for the stratospheric aerosol, *Science*, *270*, 1650-1653, 1995.
- Carlson, R. W., et al., Galileo infrared imaging spectroscopy measurements at Venus, *Science*, *253*, 1541-1548, 1991.

- Chimonas, G., The extension of the Miles-Howard theorem to compressible fluids, *J. Fluid Mech.*, *43*, 833-836, 1970.
- Chimonas, G., and J. R. Grant, Shear excitation of gravity waves, II, Upscale scattering from Kelvin-Helmholtz waves, *J. Atmos. Sci.*, *41*, 2278-2288, 1984.
- Collard, A. D., F. W. Taylor, S. B. Calcutt, R. W. Carlson, L. W. Kamp, K. H. Baines, Th. Encrenaz, P. Drossart, E. Lellouch, and B. Bézard, Latitudinal distributions of carbon monoxide in the deep atmosphere of Venus, *Planet. Space Sci.*, *41*, 487-494, 1993.
- Counselman III, C. C., S. A. Gourevitch, R. W. King, and G. B. Lorient, Zonal and meridional circulation of the lower atmosphere of Venus determined by radio interferometry, *J. Geophys. Res.*, *85*, 8026-8030, 1980.
- Crisp, D., Radiative forcing of the Venus mesosphere, II, *Icarus*, *77*, 391-413, 1989.
- Crisp, D., S. McMuldroy, S. K. Stephens, W. M. Sinton, B. Regent, K.-W. Hodapp, R. G. Probst, L. R. Doyle, D. A. Allen, and J. Elias, Ground-based near-infrared imaging observations of Venus during the Galileo encounter, *Science*, *253*, 1538-1541, 1991.
- Davis, P. A., and W. R. Peltier, Resonant parallel shear instability in the stably stratified planetary boundary layer, *J. Atmos. Sci.*, *33*, 1287-1330, 1976.
- Davis, P. A., and W. R. Peltier, Some characteristics of the Kelvin-Helmholtz and resonant overreflection modes of shear flow instability and of their interaction through vortex pairing, *J. Atmos. Sci.*, *36*, 2394-2412, 1979.
- Del Genio, A. D., and W. B. Rossow, Planetary-scale waves and the cyclic nature of cloud top dynamics on Venus, *J. Atmos. Sci.*, *47*, 293-318, 1990.
- Del Genio, A. D., W. Zhou, and T. P. Eichler, Equatorial superrotation in a slowly rotating GCM: implications for Titan and Venus, *Icarus*, *101*, 1-17, 1993.
- DeMore, W. B., S. P. Sander, D. M. Golden, R. F. Hampson, M. J. Kurylo, C. J. Howard, A. R. Ravishankara, C. E. Kolb, M. J. Molina, *Chemical Kinetics and Photochemical Data for Use in Stratospheric Modeling, Evaluation Number 12*, JPL Publication 97-4, Jet Propulsion Laboratory, 1997.

- Dickinson, R. E., Infrared radiative heating and cooling in the Venusian mesosphere. 1: global mean radiative equilibrium, *J. Atmos. Sci.*, 29, 1531-1556, 1972.
- Donahue, T. M., and R. R. Hodges Jr., Past and present water budget of Venus, *J. Geophys. Res.*, 97, 6083-6091, 1992.
- Drossart, P., B. Bézard, Th. Encrenaz, E. Lellouch, M. Roos, F. W. Taylor, A. D. Collard, S. B. Calcutt, J. Pollack, D. H. Grinspoon, R. W. Carlson, K. H. Baines, and L. W. Kamp, Search for spatial variations of the H<sub>2</sub>O abundance in the lower atmosphere of Venus from NIMS-Galileo, *Planet. Space Sci.*, 41, 495-504, 1993.
- Eisenberg, D., and W. Kauzmann, *The structure and properties of water*, Oxford, London, 1969.
- Encrenaz, Th, E. Lellouch, J. Cernicharo, G. Paubert, S. Gulikis, and T. Spilker, The thermal profile and water abundance in the Venus mesosphere from H<sub>2</sub>O and HDO millimeter observations, *Icarus*, 117, 162-172, 1995.
- Esposito, L. W., R. G. Knollenberg, M. Y. Marov, O. B. Toon, and R. P. Turco, The clouds and hazes of Venus, in *Venus*, edited by D. M. Hunten, L. Colin, T. M. Donahue, and V. I. Moroz, pp.484-564, Univ. of Ariz. Press, Tucson, 1983.
- Fegley, B. Jr., M. Y. Zolotov, and K. Lodders, The oxidation state of the lower atmosphere and surface of Venus, *Icarus*, 125, 416-439, 1997.
- Fels, S. B., and R. S. Lindzen, The interaction of thermally excited gravity waves with mean flow, *Geophys. Fluid Dyn.*, 6, 149-191, 1974.
- Fels, S. B., A parameterization of scale-dependent radiative damping rates in the middle atmosphere, *J. Atmos. Sci.*, 39, 1141-1152, 1982.
- Fels, S. B., The radiative damping of short vertical scale waves in the mesosphere, *J. Atmos. Sci.*, 41, 1755-1764, 1984.
- Fels, S. B., An approximate analytical method for calculating tides in the atmosphere of Venus, *J. Atmos. Sci.*, 43, 2757-2772, 1986.
- Fink, U., H. P. Larson, G. P. Kuiper, and R. F. Poppen, Water vapor in the atmosphere of Venus, *Icarus*, 17, 617-631, 1972.

- Fritts, D. C., Shear excitation of atmospheric gravity waves, *J. Atmos. Sci.*, *39*, 1936-1952, 1982.
- Gierasch, P. J., Meridional circulation and the maintenance of the Venus atmospheric rotation, *J. Atmos. Sci.*, *32*, 1038-1044, 1975.
- Garcia, R. R. and S. Solomon, The effect of breaking gravity waves on the dynamics and chemical composition of the mesosphere and lower thermosphere, *J. Geophys. Res.*, *90*, 3850-3868, 1985.
- Greeley, R. et al., Aeolian features on Venus, preliminary Magellan results, *J. Geophys. Res.*, *97*, 13319-13345, 1992.
- Greeley, R., K. Bender, and P. E. Thomas, Wind-related features and processes on Venus: summary of Magellan results, *Icarus*, *115*, 399-420, 1995.
- Hamill, P., E. J. Jensen, P. B. Russell, and J. J. Bauman, The life cycle of stratospheric aerosol particles, *Bull. Amer. Meteor. Soc.*, *78*, 1395-1410, 1997.
- Hansen, J. E., and J. W. Hovenier, Interpretation of the polarization of Venus, *J. Atmos. Sci.*, *31*, 1137-1160, 1974.
- Hanson, W. B., S. Sanatani and D. R. Zuccaro, The Martian ionosphere as observed by the Viking retarding potential analyzers, *J. Geophys. Res.*, *82*, 4351-4363, 1977.
- Hshimoto, G. L., Potential variability of albedo on Venus: impact on climate evolution, Master's thesis, University of Tokyo, 1996.
- Haynes, P. H., and M. E. McIntyre, On the evolution of vorticity and potential vorticity in the presence of diabatic heating and frictional or other forces, *J. Atmos. Sci.*, *44*, 828-841, 1987.
- Haynes, P. H., C. J. Marks, M. E. McIntyre, T. G. Shepherd, and K. P. Shine, On the "downward control" of extratropical diabatic circulations by eddy-induced mean zonal forces, *J. Atmos. Sci.*, *48*, 651-678, 1991.
- Hedin, A. E., H. B. Niemann, W. T. Kasprzak and A. Seiff, Global empirical model of the Venus thermosphere, *J. Geophys. Res.*, *88*, 73-83, 1983.
- Hines, C. O., Internal atmospheric gravity waves at ionospheric heights, *Can. J. Phys.*, *38*, 1441-1481, 1960.

- Hinson, D. P., and J. M. Jenkins, Magellan radio occultation measurements of atmospheric waves on Venus, *Icarus*, 114, 310-327, 1995.
- Hodges, R. R. Jr., Radiative decay in carbon dioxide, *J. Geophys. Res.*, 74, 862-867, 1969.
- Holton, J. R., P. H. Haynes, M. E. McIntyre, A. R. Douglass, R. B. Rood, and L. Pfister, Stratosphere-troposphere exchange, *Rev. Geophys.*, 33, 403-439, 1995.
- Hou, A. Y., and R. M. Goody, Diagnostic requirements for the superrotation on Venus, *J. Atmos. Sci.*, 42, 413-432, 1981.
- Hou, A. Y., and B. F. Farrell, Superrotation induced by critical-level absorption of gravity waves on Venus: An assessment, *J. Atmos. Sci.*, 44, 1049-1061, 1987.
- Hou, A. Y., and R. M. Goody, Further studies of the circulation of the Venus atmosphere, *J. Atmos. Sci.*, 46, 991-1001, 1989.
- Hou, A. Y., S. B. Fels, and R. M. Goody, Zonal superrotation above Venus' cloud base induced by the semidiurnal tide and the mean meridional circulation, *J. Atmos. Sci.*, 47, 1894-1901, 1990.
- Ignatiev, N. I., V. I. Moroz, B. E. Moshkin, A. P. Ekonomov, V. I. Gnedykh, A. V. Grigoriev, and I. V. Khatuntsev, Water vapor in the lower atmosphere of Venus: a new analysis of optical spectra measured by entry probes, *Planet. Space Sci.*, 45, 427-438, 1997.
- Imamura, T., and T. Ogawa, Radiative damping of gravity waves in the terrestrial planetary atmospheres, *Geophys. Res. Lett.*, 22, 267-270, 1995.
- Imamura, T., Momentum balance of the Venusian midlatitude mesosphere, *J. Geophys. Res.*, 102, 6615-6620, 1997.
- A. P. Ingersoll, D. Crisp, A. W. Grossman, and the VEGA balloon science team, Estimates of convective heat fluxes and gravity wave amplitudes in the Venus middle cloud layer from VEGA balloon measurements, *Adv. Space Res.*, 7(12), 343-349, 1987.
- Iversen, J. D., R. Greeley, and J. B. Pollack, Windblown dust on Earth, Mars and Venus, *J. Atmos. Sci.*, 33, 2425-2429, 1976.

- James, E. P., O. B. Toon, and G. Schubert, A numerical microphysical model of the condensational Venus cloud, *Icarus*, *129*, 147-171, 1997.
- Jenkins, J. M., and P. G. Steffes, Results for 13-cm absorptivity and H<sub>2</sub>SO<sub>4</sub> abundance profiles from the season 10 (1986) Pioneer Venus orbiter radio occultation experiment, *Icarus*, *90*, 129-138, 1991.
- Jenkins, J. M., P. G. Steffes, D. P. Hinson, J. D. Twicken, and G. L. Tyler, Radio occultation studies of the Venus atmosphere with the Magellan spacecraft, 2. results from the October 1991 experiments, *Icarus*, *110*, 79-94, 1994.
- Joshi, M. M., B. N. Lawrence, and S. R. Lewis, Gravity wave drag in three-dimensional atmospheric models of Mars, *J. Geophys. Res.*, *100*, 21235-21245, 1995.
- Kamp, L. W., F. W. Taylor, and S. B. Calcutt, Structure of Venus's atmosphere from modeling of night-side infrared spectra, *Nature*, *336*, 360-362, 1988.
- Kamp, L. W., and F. W. Taylor, Radiative-transfer models of the night side of Venus, *Icarus*, *86*, 510-529, 1990.
- Kawabata, K., D. L., Coffeen, J. E. Hansen, W. A. Lane, M. Sato, and L. D. Travis, Cloud and haze properties from Pioneer Venus polarimetry, *J. Geophys. Res.*, *85*, 8129-8140, 1980.
- Kaye, G. W. C., and T. H. Laby, *Tables of Physical and Chemical Constants*, London, Longmans, Green, 1986.
- Knollenberg, R. G., and D. M. Hunten, The microphysics of the clouds of Venus: results of the Pioneer Venus particle size spectrometer experiment, *J. Geophys. Res.*, *85*, 8039-8058, 1980.
- Knollenberg, R. G., A reexamination of the evidence for large, solid particles in the clouds of Venus, *Icarus*, *57*, 161-183, 1984.
- Kolodner, M. A., and P. G. Steffes, The microwave absorption and abundance of sulfuric acid vapor in the Venus atmosphere, *Bull. Amer. Astron. Soc.*, *28*, 1116-1117, 1996.
- Krasnopolsky, V. A., and V. A. Parshev, Chemical composition of the atmosphere of Venus, *Nature*, *292*, 610-613, 1981.

- Krasnopolsky, V. A., and V. A. Parshev, Photochemistry of the Venus atmosphere, in *Venus*, edited by D. M. Hunten, L. Colin, T. M. Donahue, and V. I. Moroz, pp.431-458, Univ. of Ariz. Press, Tucson, 1983.
- Krasnopolsky, V. A., *Photochemistry of the Atmospheres of Mars and Venus*, Springer-Verlag, 1986.
- Krasnopolsky, V. A., and J. B. Pollack, H<sub>2</sub>O-H<sub>2</sub>SO<sub>4</sub> system in Venus' clouds and OCS, CO, and H<sub>2</sub>SO<sub>4</sub> profiles in Venus' troposphere, *Icarus*, 109, 58-78, 1994.
- Kulmala, M., and A. Laaksonen, Binary nucleation of water-sulfuric acid system: comparison of classical theories with different H<sub>2</sub>SO<sub>4</sub> saturation vapor pressures, *J. Chem. Phys.*, 93, 696-701, 1990.
- Leroy, S. S., and A. P. Ingersoll, Radio scintillations in Venus's atmosphere: Application of a theory of gravity wave generation, *J. Atmos. Sci.*, 53, 1018-1028, 1996.
- Lindzen, R. S., Turbulence and stress owing to gravity wave and tidal breakdown, *J. Geophys. Res.*, 86, 9707-9714, 1981.
- Llewellyn, E. J, I. C. McDade, P. Moorhouse and M. D. Lockertie, Possible reference models for atomic oxygen in the terrestrial atmosphere, *Adv. Space Res.*, 13, (1)135-144, 1993.
- Lovejoy, E. R., D. R. Hanson, and L. G. Huey, Kinetics and products of the gas-phase reaction of SO<sub>3</sub> with water, *J. Phys. Chem.*, 100, 19911-19916, 1996.
- Mauson, A. H., Gravity wave horizontal and vertical wavelengths: an update of measurements in the mesopause region (~80-100 km), *J. Atmos. Sci.*, 47, 2765-2773, 1990.
- Matsuda, Y., Dynamics of the four-day circulation in the Venus atmosphere, *J. Meteor. Soc. Japan*, 58, 443-470, 1980.
- McElroy, M. B., T. Y. Kong and Y. L. Yung, Photochemistry and evolution of Mars' atmosphere: a Viking perspective, *J. Geophys. Res.*, 82, 4379-4388, 1977.
- McIntyre, M. E., and M. A. Weissman, On radiating instabilities and resonant overreflection, *J. Atmos. Sci.*, 35, 1190-1196, 1978.

- McIntyre, M. E., On dynamics and transport near the polar mesopause in summer, *J. Geophys. Res.*, *94*, 14,617-14,628, 1989.
- Meadows, V. S., and D. Crisp, Ground-based near-infrared observations of the Venus nightside, the thermal structure and water abundance near the surface, *J. Geophys. Res.*, *101*, 4595-4622, 1996.
- Moroz, V. I., The atmosphere of Venus, *Space Sci. Rev.*, *29*, 3-127, 1981.
- Murayama, Y., T. Tsuda, and S. Fukao, Seasonal variation of gravity wave activity in the lower atmosphere observed with the MU radar, *J. Geophys. Res.*, *99*, 23,057-23,069, 1994.
- Murray, B. C., M. J. S. Belton, G. E. Danielson, M. E. Davies, D. Gault, B. Hapke, B. O'Leary, R. G. Strom, V. Suomi and N. Trask, *Science* *183*, 1307-1315, 1974.
- Newman, M., G. Schubert, A. J. Kliore, and I. R. Patel, Zonal winds in the middle atmosphere of Venus from Pioneer Venus radio occultation data, *J. Atmos. Sci.*, *41*, 1901-1913, 1984.
- Newman, M., and C. Leovy, Maintenance of strong rotational winds in Venus' middle atmosphere by thermal tides, *Science*, *257*, 647-650, 1992.
- Nier, A. O. and M. B. McElroy, Composition and structure of Mars' upper atmosphere: results from the neutral mass spectrometers on Viking 1 and 2, *J. Geophys. Res.*, *82*, 4341-4349, 1977.
- Oyama, V. I., G. C. Carle, F. Woeller, J. B. Pollack, R. T. Reynolds, and R. A. Craig, Pioneer Venus gas chromatography of the lower atmosphere of Venus, *J. Geophys. Res.*, *85*, 7891-7902, 1980.
- Pollack, J. B., and R. Young, Calculation of the radiative and dynamical state of the Venus atmosphere, *J. Atmos. Sci.*, *32*, 1025-1037, 1975.
- Pollack, J. B., D. W. Strecker, F. C. Witteborn, E. F. Erickson, and B. J. Baldwin, Properties of the clouds of Venus, as inferred from airborne observations of its near-infrared reflectivity spectrum, *Icarus*, *34*, 28-45, 1978.
- Pollack, J. B., O. B. Toon, and R. Boese, Greenhouse models of Venus's high surface temperature, as constrained by Pioneer Venus measurements, *J. Geophys. Res.*, *85*, 8223-8231, 1980.

- Pollack, J. B., J. B. Dalton, D. Grinspoon, R. B. Wattson, R. Freedman, D. Crisp, D. A. Allen, B. Bezard, C. DeBergh, L. P. Giver, Q. Ma, and R. Tipping, Near-infrared light from Venus' nightside. a spectroscopic analysis, *Icarus*, 103, 1-42, 1993.
- Prinn, R. G., Venus: chemistry of the lower atmosphere prior to the Pioneer Venus mission, *Geophys. Res. Lett.*, 5, 973-976, 1978.
- Reed, R. A., W. J. Forrest, J. R. Houck, and J. B. Pollack, Venus: the 17- to 38-micron spectrum, *Icarus*, 33, 554-557, 1978.
- Revercomb, H. E., L. A. Sromovsky, V. E. Suomi, and R. W. Boese, Net thermal radiation in the atmosphere of Venus, *Icarus*, 61, 521-538, 1985.
- Rodgers, C. D., F. W. Taylor and A. H. Muggerridge, Local thermodynamic equilibrium of carbon dioxide in the upper atmosphere, *Geophys. Res. Lett.*, 19, 589-592, 1992.
- Rossow, W. B., and G. P. Williams, Large scale motion in the Venus stratosphere, *J. Atmos. Sci.*, 36, 377-389, 1979.
- Rossow, W. B., A. D. Del Genio, S. S. Limaye and L. D. Travis, Cloud morphology and motions from Pioneer Venus images, *J. Geophys. Res.*, 85, 8107-8128, 1980.
- Rossow, W. B., A. D. Del Genio, S. S. Limaye, and L. D. Travis, Cloud morphology and motions from Pioneer Venus images, *J. Geophys. Res.*, 85, 8107-8128, 1980.
- Rossow, W. B., A general circulation model of a Venus-like atmosphere, *J. Atmos. Sci.*, 40, 273-302, 1983.
- Rossow, W. B., A. D. Del Genio, and T. Eichler, Cloud-tracked winds from Pioneer Venus OCPP images, *J. Atmos. Sci.*, 47, 2053-2084, 1990.
- Rothman, L. S., R. R. Gamache, R. H. Tipping, C. P. Rinsland, M. A. H. Smith, D. C. Benner, V. M. Devi, J. -M. Flaud, L. R. Brown and R. A. Toth, The Hitran molecular database: editions of 1991 and 1992, *J. Quant. Spectrosc. Radiat. Transfer*, 48, 469-507, 1992.
- Schofield, J. T., F. W. Taylor, and D. J. McCleese, The global distribution of water vapor in the middle atmosphere of Venus, *Icarus*, 52, 263-278, 1982.
- Seiff, A. and D. B. Kirk, Structure of the atmosphere of Mars in summer at mid-latitudes, *J. Geophys. Res.*, 82, 4364-4378, 1977.

- Seiff, A., D. B. Kirk, R. E. Young, R. C. Blanchard, J. T. Findlay, G. M. Kelly, and S. C. Sommer, Measurements of thermal structure and thermal contrasts in the atmosphere of Venus and related dynamical observations: Results from the four Pioneer probes, *J. Geophys. Res.*, *85*, 7903-7933, 1980.
- Seiff, A., J. T. Schofield, A. J. Kliore, F. W. Taylor, S. S. Limaye, H. E. Revercomb, L. A. Stromovsky, V. V. Kerzhanovich, V. I. Moroz and M. Y. Marov, Models of the structure of the atmosphere of Venus from the surface to 100 kilometers altitude, *Adv. Space Res.* *5* (No. 11), 3-58, 1985.
- Schubert, G., C. Covey, A. Del Genio, L. S. Elson, G. Keating, A. Seiff, R. E. Young, J. Apt, C. C. Counselman III, A. J. Kliore, S. S. Limaye, H. E. Revercomb, L. A. Stromovsky, V. E. Suomi, F. Taylor, R. Woo, and U. von Zahn, Structure and circulation of the Venus atmosphere, *J. Geophys. Res.*, *85*, 8007-8025, 1980.
- Schubert, G., and R. L. Walterscheid, Propagation of small-scale acoustic-gravity waves in the Venus atmosphere, *J. Atmos. Sci.*, *41*, 1202-1213, 1984.
- Schubert, G., General circulation and dynamical state of the Venus atmosphere, *Venus*, edited by D. M. Hunten, L. Colin, T. M. Donahue, and V. I. Moroz, pp.650-680, Univ. of Ariz. Press, Tucson, 1983.
- Seiff, A., D. B. Kirk, R. E. Young, R. C. Blanchard, J. T. Findlay, G. M. Kelly, and S. C. Sommer, Measurements of thermal structure and thermal contrasts in the atmosphere of Venus and related dynamical observations, results from the four Pioneer Venus probes, *J. Geophys. Res.*, *85*, 7903-7933, 1980.
- Seiff, A., Thermal structure of the atmosphere of Venus, *Venus*, edited by D. M. Hunten, L. Colin, T. M. Donahue, and V. I. Moroz, pp.215-279, Univ. of Ariz. Press, Tucson, 1983.
- Seiff, A., J. T. Schofield, A. J. Kliore, F. W. Taylor, S. S. Limaye, H. E. Revercomb, L. A. Stromovsky, V. V. Kerzhanovich, V. I. Moroz, and M. Y. Marov, Models of the structure of the atmosphere of Venus from the surface to 100 kilometers altitude, *Adv. Space Res.*, *5*(11), 3-58, 1985.
- Seiff, A., and D. B. Kirk, Waves in Venus' middle and upper atmosphere: Implications of Pioneer Venus probe data above the clouds, *J. Geophys. Res.*, *96*, 11,021-11,032, 1991.

- Sharma, R. D. and P. P. Wintersteiner, Role of carbon dioxide in cooling planetary thermospheres, *Geophys. Res. Lett.*, 17, 2201-2204, 1990.
- Shia, R. -L., Y. L. Yung, M. Allen, R. W. Zurek, and D. Crisp, Sensitivity study of advection and diffusion coefficients in a two-dimensional stratospheric model using excess carbon 14 data, *J. Geophys. Res.*, 94, 18467-18489, 1989.
- Spiegel, E. A., The smoothing of temperature fluctuations by radiative transfer, *Astrophys. J.* 126, 202-207, 1957.
- Stone, P. H., The structure and circulation of the deep Venus atmosphere, *J. Atmos. Sci.*, 31, 1681-1690, 1974.
- Stone, P. H., The dynamics of the atmosphere of Venus, *J. Atmos. Sci.*, 32, 1005-1016, 1975.
- Sutherland, B. R., and W. R. Peltier, Turbulence transition and internal wave generation in density stratified jets, *Phys. Fluids*, 6, 1267-1284, 1994.
- Taylor, F. W., R. Beer, M. T. Chahine, D. J. Diner, L. S. Elson, R. D. Haskins, D. J. McCleese, J. V. Martonchik, and P. E. Reichley, Structure and meteorology of the middle atmosphere of Venus: Infrared remote sensing from the Pioneer orbiter, *J. Geophys. Res.*, 85, 7963-8006, 1980.
- Taylor, F. W., D. M. Hunten, and L. V. Ksanfomaliti, The thermal balance of the middle and upper atmosphere of Venus, in *Venus*, edited by D. M. Hunten, L. Colin, T. M. Donahue, and V. I. Moroz, pp.650-680, Univ. of Ariz. Press, Tucson, 1983.
- Tomasko, M. G., The thermal balance of the lower atmosphere of Venus, in *Venus*, edited by D. M. Hunten, L. Colin, T. M. Donahue, and V. I. Moroz, pp.604-631, Univ. of Ariz. Press, Tucson, 1983.
- Toon, O. B., B. Ragent, D. Colburn, J. Blamont, and C. Cot, Large, solid particles in the clouds of Venus: do they exist ?, *Icarus*, 57, 143-160, 1984.
- Travis, L. D., Nature of the atmospheric dynamics on Venus from power spectrum analysis of Mariner 10 images, *J. Atmos. Sci.*, 35, 1584-1595, 1978.
- Trepte, C. R., and M. H. Hitchman, Tropical stratospheric circulation deduced from satellite aerosol data, *Nature*, 355, 626-628, 1992.

- von Zahn, U., S. Kumar, H. Niemann, and R. Prinn, Composition of the Venus atmosphere, in *Venus*, edited by D. M. Hunten, L. Colin, T. M. Donahue, and V. I. Moroz, pp.484-564, Univ. of Ariz. Press, Tucson, 1983.
- Weinstock, J., Nonlinear theory of acoustic-gravity waves I. saturation and enhanced diffusion, *J. Geophys. Res.*, *81*, 633-652, 1976.
- Winick, J. R., and A. I. F. Stewart, Photochemistry of SO<sub>2</sub> in Venus' upper cloud layers, *J. Geophys. Res.*, *85*, 7849-7860, 1980.
- Woo, R., and A. Ishimaru, Eddy diffusion coefficient for the atmosphere of Venus from radio scintillation measurement, *Nature*, *289*, 383-384, 1981.
- Woo, R., J. W. Armstrong, and A. J. Kliore, Small-scale turbulence in the atmosphere of Venus, *Icarus*, *52*, 335-345, 1982.
- Yang, H., K. K. Tung, and E. Olagner, Nongeostrophic theory of zonally averaged circulation. part II: Eliassen-Palm flux divergence and isentropic mixing coefficient, *J. Atmos. Sci.*, *47*, 215-241, 1990.
- Young, A. T., Are the clouds on Venus sulfuric acid ?, *Icarus*, *18*, 564-582, 1973.
- Young, L. D. G., High resolution spectra of Venus - a review, *Icarus*, *17*, 632-658, 1972.
- Young, R. E., R. L. Walterscheid, G. Schubert, L. Pfister, H. Houben, and D. L. Bindshadler, Characteristics of finite amplitude stationary gravity waves in the atmosphere of Venus, *J. Atmos. Sci.*, *51*, 1857-1875, 1994.
- Yung, Y. L., and W. B. DeMore, Photochemistry of the stratosphere of Venus: implications for atmospheric evolution, *Icarus*, *51*, 199-247, 1982.
- Zeleznik, F. J., Thermodynamic properties of the aqueous sulfuric acid system to 350 K, *J. Phys. Chem. Ref. Data*, *20*, 1157-1200, 1991.
- Zhang, S., and S. W. Bougher, The impact of gravity waves on the Venus thermosphere and O<sub>2</sub> IR nightglow, *J. Geophys. Res.*, *101*, 23105-23205, 1996.
- Zhu, X., Radiative damping revisited: parameterization of damping rate in the middle atmosphere, *J. Atmos. Sci.*, *50*, 3008-3021, 1993.
- Zhu, X. and D. F. Strobel, Radiative damping in the upper atmosphere, *J. Atmos. Sci.*, *48*, 184-198, 1991.



